

Planned products of the Mars Structure Service for the InSight mission to Mars

Mark P. Panning¹ · Philippe Lognonné² ·
W. Bruce Banerdt³ · Raphaël Garcia⁴ ·
Matthew Golombek³ · Sharon Kedar³ ·
Brigitte Knapmeyer-Endrun⁵ · Antoine
Mocquet⁶ · Nick A. Teanby⁷ · Jeroen
Tromp⁸ · Renee Weber⁹ · Eric Beucler⁶ ·
Jean-Francois Blanchette-Guertin² · Ebru
Bozdağ¹⁰ · Mélanie Drilleau² · Tamara
Gudkova^{11,12} · Stefanie Hempel⁴ · Amir
Khan¹³ · Vedran Lekić¹⁴ · Naomi
Murdoch⁴ · Ana-Catalina Plesa¹⁵ ·
Atilio Rivoldini¹⁶ · Nicholas Schmerr¹⁴ ·
Youyi Ruan⁸ · Olivier Verhoeven⁶ ·
Chao Gao¹⁴ · Ulrich Christensen⁵ ·
John Clinton¹⁷ · Veronique Dehant¹⁶ ·
Domenico Giardini¹³ · David
Mimoun⁴ · W. Thomas Pike¹⁸ · Sue
Smrekar³ · Mark Wieczorek² · Martin
Knapmeyer¹⁵ · James Wookey⁷

Received: 18 July 2016 / Accepted: 16 November 2016 / doi: 10.1007/s11214-016-0317-5

M.P. Panning

E-mail: mpanning@ufl.edu

¹ Department of Geological Sciences, University of Florida, 241 Williamson Hall, Box 112120, Gainesville, FL 32611, United States

² Univ Paris Diderot-Sorbonne Paris Cité, Institut de Physique du Globe de Paris, 35 rue Hélène Brion - Case 7071, Lamarck A - 75205 Paris Cedex 13, France

³ Jet Propulsion Laboratory, California Institute of Technology, 4800 Oak Grove Drive, Pasadena, CA 91109, United States

⁴ Institut Supérieur de l'Aéronautique et de l'Espace, Toulouse, France

⁵ Max Planck Institute for Solar System Research, Justus-von-Liebig-Weg 3, 37077 Göttingen, Germany

⁶ Laboratoire de Planétologie et Géodynamique, UMR-CNRS 6112, Université de Nantes, Faculté des Sciences et Techniques, 2 rue de la Houssinière - BP 92208, 44322 Nantes Cedex 3, France

⁷ School of Earth Sciences, University of Bristol, Wills Memorial Building, Queens Road, Bristol BS8 1RJ, United Kingdom

⁸ Department of Geosciences, Princeton University, Princeton, New Jersey, United States

⁹ NASA Marshall Space Flight Center, 320 Sparkman Drive, Huntsville, AL 35805, United States

¹⁰ Géoazur, University of Nice Sophia Antipolis, 250 rue Albert Einstein, 06560 Valbonne, France

Abstract The InSight lander will deliver geophysical instruments to Mars in 2018, including seismometers installed directly on the surface (Seismic Experiment for Interior Structure, SEIS). Routine operations will be split into two services, the Mars Structure Service (MSS) and Marsquake Service (MQS), which will be responsible, respectively, for defining the structure models and seismicity catalogs from the mission. The MSS will deliver a series of products before the landing, during the operations, and finally to the Planetary Data System (PDS) archive. Prior to the mission, we assembled a suite of *a priori* models of Mars, based on estimates of bulk composition and thermal profiles. Initial models during the mission will rely on modeling surface waves and impact-generated body waves independent of prior knowledge of structure. Later modeling will include simultaneous inversion of seismic observations for source and structural parameters. We use Bayesian inversion techniques to obtain robust probability distribution functions of interior structure parameters. Shallow structure will be characterized using the hammering of the heatflow probe mole, as well as measurements of surface wave ellipticity. Crustal scale structure will be constrained by measurements of receiver function and broadband Rayleigh wave ellipticity measurements. Core interacting body wave phases should be observable above modeled martian noise levels, allowing us to constrain deep structure. Normal modes of Mars should also be observable and can be used to estimate the globally averaged 1D structure, while combination with results from the InSight radio science mission and orbital observations will allow for constraint of deeper structure.

Keywords Mars · seismology · interior structure · InSight mission

1 Introduction

In order to obtain detailed information on planetary interiors, surface geophysical observations in general, and seismological measurements in particular are of critical importance (e.g. Lognonné and Johnson, 2007). Much of our knowledge of the internal structure of the planetary bodies in our solar system is achieved through observations such as gravity field, rotation, and tides obtained by precisely tracking orbiting spacecraft or landers on the planets surface, but those observations provide an integrated view of interiors which

¹¹ Schmidt Institute of Physics of the Earth, Russian Academy of Sciences, B.Gruzinskaya, 10, Moscow 123495, Russia

¹² Moscow Institute of Physics and Technology (MIPT), Institutsky per., 9, Moscow region, 141700, Russia

¹³ Institut für Geophysik, ETH Zürich, 8092 Zürich, Switzerland

¹⁴ Department of Geology, University of Maryland, College Park, MD 20742, United States

¹⁵ German Aerospace Center (DLR), Rutherfordstrasse 2, 12489 Berlin, Germany

¹⁶ Royal Observatory Belgium, Av Circulaire 3-Ringlaan 3, 1180 Brussels, Belgium

¹⁷ Swiss Seismological Service, ETH Zürich, 8092 Zürich, Switzerland

¹⁸ Department of Electrical and Electronic Engineering, Imperial College, London, United Kingdom

is generally non-unique. For the Earth, on the other hand, we have a detailed picture of the interior primarily obtained through the study of seismic data.

Prior to the first recording of global scale seismograms by Von Rebeur-Paschwitz (Von Rebeur-Paschwitz, 1889), the best information on the Earth's internal structure was determined from Earth tide analysis (Thomson, 1863; Darwin, 1882). After the advent of quality seismometers in the late 19th and early 20th centuries, our knowledge of Earth structure expanded rapidly with the discovery of the core by Richard Oldham in 1906, the crust-mantle discontinuity by Andrija Mohorovičić in 1909, and the inner core by Inge Lehmann in 1936. By 1939, Harold Jeffreys had produced a 1D global model of the whole Earth capable of matching P wave arrivals within 0.2% (see e.g. Lay and Wallace, 1995, ch. 1). The only other planetary body, however, for which we have obtained seismic data unambiguously containing signals from the interior is the Earth's moon. The data from seismometers deployed on the Moon as part of Apollo Passive Seismic Experiment by astronauts in five of the six Apollo missions between 1969 and 1972, which recorded data until 1977, gave first order constraints on lunar interior structure, while also producing very unexpected seismograms showing high levels of scattering (e.g. Nakamura, 1983). Perhaps the best illustration of the power of such scarce planetary seismic data is the number of studies in recent years based on the Apollo data that have continued to update our understanding of the lunar interior, including observations of the core and possible deep partial melt, despite not receiving any new data since the 70's (Khan and Mosegaard, 2002; Lognonné et al, 2003; Chenet et al, 2006; Gagnepain-Beyneix et al, 2006; Khan et al, 2007; Weber et al, 2011; Garcia et al, 2011; Zhao et al, 2012; Steinberger et al, 2015; Matsumoto et al, 2015).

The planned InSight lander mission to Mars (Banerdt et al, 2013) will extend planetary seismology to Mars, and enable other surface geophysical measurements to determine details of the internal structure and evolution of another terrestrial planet for the first time. The mission will include 3-component broadband and short period seismometers (Seismic Experiment for Interior Structure, SEIS, Lognonné et al, 2012; Mimoun et al, 2012; Lognonné and Pike, 2015), as well as a heat flow probe (Heat flow and Physical Properties Probe, HP³, Spohn et al, 2014), a geodetic experiment (Rotation and Interior Structure Experiment, RISE, Folkner et al, 2012), and a magnetometer, in addition to meteorological sensors.

While 2 seismometers were landed on Mars during the Viking missions in the late 1970's, the seismometer on Viking 1 did not properly uncage, and the placement of the seismometer on the top of the Viking 2 lander prevented the recovery of any signals definitively originating in the planetary interior (Anderson et al, 1977). Twenty years later, a second unsuccessful attempt was made with the OPTIMISM seismometers (Lognonné et al, 1998) onboard 2 Small Autonomous Stations (Linkin et al, 1998) of the failed Mars96 mission. The placement of the sensitive SEIS instrument package directly on the surface of Mars by the InSight lander, however, is likely to usher in a new era of planetary seismology, enabling broadband seismology and the recording of

seismic and gravimetric signals from tidal frequencies up to high frequency seismic waves at 50 Hz .

The primary science deliverables from the SEIS instrument are internal structure models of Mars and a seismicity catalog defining activity on Mars. To that end, the SEIS team has formed two main services for the mission: the Mars Structure Service (MSS) to focus on defining the internal structure models and the Marsquake Service (MQS) to catalog the detected marsquakes and impacts. While the two tasks are intimately related and will require constant feedback and interaction, these two services provide a structure to ensure the mission will meet its science goals. In this paper, we describe the major anticipated products of the MSS starting from pre-launch models through initial modeling and refinement as more data becomes available through the nominal 2 year duration of the mission. This is meant primarily to serve as a high level overview and summary of the published and ongoing research being done on these topics by researchers within the MSS, and more detailed descriptions can be found for most techniques and products in the included references. In the following sections, we detail the products already produced and planned in advance of the mission (section 2) and anticipated products early in the monitoring phase of the mission (section 3). We then detail the final anticipated products relating to structure from the local shallow subsurface (section 4), crust and shallow mantle (section 5), deep mantle and core (section 6), and planetary scale normal modes and tides (section 7).

2 Pre-launch estimates of structure and seismicity

Prior to launch, both the MSS and MQS have been active in gathering available *a priori* estimates of martian structure and seismicity. This is an essential process for a variety of reasons. Adequate estimates of sources and structure define our expectations for the types of signals we will recover from the surface of Mars, which is an important input going into the final instrument and lander software design that will be launched. Also, such models are critical inputs to aid in software development for data processing to recover source and structure parameters when real martian data becomes available. Without a doubt, aspects of martian seismograms will present unexpected challenges; nevertheless, the goal of both services is to have mature algorithms and software to handle the incoming data as efficiently as possible.

2.1 Structure estimates

Despite the lack of seismic observational data, basic constraints from planetary mass, moment of inertia, and tidal Love number k_2 (e.g. Genova et al, 2016; Konopliv et al, 2016, for recent estimates), combined with some assumptions on bulk chemistry based on constraints primarily from martian meteorites (McSween, 1994; Taylor, 2013), allow for several estimates of the internal elastic and compositional structure of Mars (e.g. Mocquet et al, 1996; Sohl and

Spohn, 1997; Gudkova and Zharkov, 2004; Khan and Connolly, 2008; Zharkov et al, 2009; Rivoldini et al, 2011).

In preparation for the mission, the InSight science team has developed a suite of consistently calculated *a priori* models to reflect reasonable ranges of initial composition estimates and thermal profiles (fig. 1). From these, assuming thermodynamic equilibrium, we can calculate seismic properties using first thermodynamics principles with experimentally derived parameters for candidate mantle minerals. A range of different compositions from the literature are used (table 1), and a hot and cold end member temperature profiles (fig. 2) computed from thermal evolution models (Plesa et al, 2016). The seismic properties are calculated using the code `Perple_X` (Connolly, 2005) with the thermodynamic formulation and parameters of Stixrude and Lithgow-Bertelloni (2011) for the mantle and using the thermodynamical model developed by Rivoldini et al (2011) for the core. Figure 1 shows the shear wave velocity distribution in the martian mantle calculated for the compositions of table 1, including 5 different models of martian mantle composition. While no single model is definitive, the suite of derived models can be used in pre-launch testing, and demonstrate the base expectations we have for structure prior to return of actual seismic data from InSight.

2.2 Estimates of likely sources

While the seismic catalog will be produced by the other major service of the mission, the MQS, pre-launch estimates of seismicity are also extremely important for defining the techniques that will be useful to determine the structure models. Mars' seismicity is expected to lie somewhere between that of the Earth and the Moon, with potential sources including faulting, meteorite impacts, and atmospheric hum (Golombek et al, 1992; Lognonné and Mosser, 1993; Lognonné et al, 1996; Panning et al, 2015). The Phobos tide is another signal with known amplitude, which can be expected to be detected through stacking (Lognonné and Mosser, 1993; Lognonné et al, 2000; Van Hoolst et al, 2003).

The total seismic moment release per year is 10^{22} Nm/yr on the Earth and 10^{15} Nm/yr on the Moon, which loosely brackets the total moment release on Mars to be between 10^{17} Nm/yr and 10^{19} Nm/yr (Golombek, 2002). Faulting, driven by internal cooling and large lithospheric loads such as Tharsis, is expected to be the dominant source of seismicity. Estimates based on predicted stress release from internal cooling (Phillips, 1991) and the area, total slip and age of surface faults (Golombek et al, 1992) both derive a total moment release for Mars of about 10^{18} Nm/yr . The largest uncertainties in deriving recurrence intervals for different magnitude seismic events center around the assumed negative power law slope of the number versus size of marsquakes and the largest possible marsquake (Golombek, 1994). Knapmeyer et al (2006) explore these uncertainties and derive a variety of possible models that vary these parameters and bracket the possibilities (fig. 3). Inter-

mediate estimates suggest ~ 100 marsquakes per year with seismic moments above 10^{13} Nm (detectable at epicentral distance $\leq 60^\circ$).

Of particular interest for InSight are the estimates for seismicity on Cerberus Fossae, one of the youngest tectonic features on Mars from which water carved catastrophic outflow channels (Athabasca Valles to the southwest and Marte Valley to the northeast) (Burr et al, 2002) and lava covered a vast portion of Elysium Planitia (Plescia, 1990; Jaeger et al, 2007; Vaucher et al, 2009). Cerberus Fossae has been interpreted as a long graben system with cumulative offsets of 500 m or more (Vetterlein and Roberts, 2010), and boulder trails young enough to be preserved in aeolian sediments, indicative of large marsquakes (Roberts et al, 2012), and estimates of moment release that indicate the likelihood of recent marsquakes large enough to be recorded by the InSight instruments (Taylor et al, 2013). Cerberus Fossae is only ~ 1500 km to the east- northeast from the InSight landing site.

Meteorites are expected to be of secondary importance compared to faulting, but have high science potential because accurate locations based on orbital imaging may be possible (Malin et al, 2006; Daubar et al, 2013). Accurate locations would significantly increase the confidence that could be placed on internal structure determinations. Early estimates by Davis (1993) predicted ~ 100 large impacts would be detectable per year with an Apollo-type seismometer. However, subsequent downward revision of the present-day meteoroid source population at Mars (Hartmann, 2005) implies that the actual number is likely to be at least an order of magnitude less than this. More recent studies using Hartmann (2005)'s updated isochrons, rescaled by a factor of 1/3 to match orbital detection rates of new craters (Malin et al, 2006; Daubar et al, 2013), suggest ~ 1 large globally detectable impact event per Earth year and 0.1–30 regionally detectable events per year (Teanby and Wookey, 2011; Teanby, 2015) depending on the seismic coupling coefficient. Lognonné and Johnson (2015) propose a rate of about 10 per year with a different approach based on the scaling of the long period seismic energy (e.g. < 1 Hz) with the impact momentum and with estimations of the frequency cutoff based on lunar observations (Lognonné et al, 2009; Gudkova et al, 2015). These estimates contain significant uncertainties, which for impacts are dominated by the large variability of seismic efficiency of the cratering process (Richardson et al, 2005). Fragmentation of small meteoroids (Williams et al, 2014) is another potential source of uncertainty, but is small compared the uncertainties introduced by seismic efficiency (Teanby, 2015).

Figure 3 shows the predicted martian seismicity discussed above compared to Earth's measured fault activity from 1990–2010. The global seismicity figures include all sources from the Harvard Centroid Moment Tensor (CMT) event catalogue, which is dominated by activity at plate boundaries. However, as plate tectonics does not operate on Mars, intra-plate activity (away from plate boundaries, subduction zones, and rifts) may be more representative. Intra-plate events from 1990–2010 in the UK and France are used as a proxy, taken from the International Seismological Centre (ISC) catalogue and converted from local magnitude to seismic moment using the relations in Hanks

and Boore (1984). The intra-plate seismicity figures are scaled up to an area equivalent to the Earth’s surface area so as to be comparable with the other estimates.

3 Modeling approach for initial velocity model delivery

The initial model delivery from MSS is expected to be complete with less than 3 months of data available from the monitoring phase. Therefore, this will need to be a model based on a limited dataset, likely with no more than 1 event large enough to record multiple orbit surface waves, or alternatively a small number of events with body wave phases and first orbit surface wave dispersion identified. When data is limited, modeling approach is very important for understanding the significance of the resulting models. Therefore, we first discuss the Bayesian framework which forms the basis for most of the planned modeling of the MSS. As examples of our proposed approach for developing these initial models, we use a signal from a non-located marsquake combined with signals from a small number of local meteoroid impacts that are located spatially, but not in time (i.e. for which we do not know the time of impact, t_0). We first invert for the S-wave velocity profile using the quake’s Rayleigh wave group velocity dispersion curve (e.g. Panning et al, 2015). We then use the impact data to compute a $V_P - V_S$ differential velocity profile. These two profiles can then be combined to retrieve a first order P wave velocity model. Finally, we also discuss modeling events with only the first Rayleigh wave train detected, both with and without considering constraints from mineral physics.

3.1 Inversion Method

We use a Markov chain Monte Carlo (MCMC) approach within a Bayesian framework. This approach goes beyond the classical computation of the unique best-fitting solution model (e.g. Mosegaard and Tarantola, 1995). This technique allows us to investigate a large range of possible models and provides a quantitative measure of the models uncertainty and non-uniqueness. As such, it is well suited to our problem given the still poorly known nature of the martian interior, as well as the initially low amount of seismic data expected. Bayesian approaches are becoming increasingly popular in planetary studies, in particular for the Moon (Khan et al, 2000; Chenet et al, 2006; Matsumoto et al, 2015), Mars (Khan and Connolly, 2008; Rivoldini et al, 2011; Panning et al, 2015; Khan et al, 2016), and Mercury (Rivoldini and Van Hoolst, 2013). For planetary applications in particular, the amount of data is likely to be relatively small compared to the Earth, and the forward problem can generally be computed with 1D structure or with relatively fast 3D forward modeling. This allows the computations of several million forward problems with modest processing powers. Such approaches have also become very prevalent in global seismology on the Earth (e.g. Shapiro and Ritzwoller, 2002; Khan et al, 2009, 2013; Bodin et al, 2012; Drilleau et al, 2013).

In our test case, the inverse problem consists of computing the V_S or $V_P - V_S$ profiles from seismological data (i. e. Rayleigh wave group velocity dispersion diagram or the difference between S and P waves' arrival times). The data \mathbf{d} are linked to the parameters \mathbf{p} through the equation $\mathbf{d} = A(\mathbf{p})$, where the non-analytic and non-linear operator A represents the forward problem. In the Bayesian framework, the solutions of the inverse problem are given by the posterior probability $P(\mathbf{p}|\mathbf{d})$ that the parameters are in a configuration \mathbf{p} given the data are in a configuration \mathbf{d} . The parameter space is sampled according to $P(\mathbf{p}|\mathbf{d})$. Bayes' theorem links the prior distribution $P(\mathbf{p})$ and the posterior distribution $P(\mathbf{p}|\mathbf{d})$,

$$P(\mathbf{p}|\mathbf{d}) = \frac{P(\mathbf{d}|\mathbf{p})P(\mathbf{p})}{\sum_{\mathbf{p} \in \mathcal{M}} P(\mathbf{d}|\mathbf{p})P(\mathbf{p})}, \quad (1)$$

where \mathcal{M} are all the configurations in the parameter space. The probability distribution $P(\mathbf{d}|\mathbf{p})$ is a function of the misfit, which estimates the difference between the observed data \mathbf{d} and the computed synthetic data $A(\mathbf{p})$. To calculate the posterior distribution (eq. 1), we use the Metropolis algorithm (e.g. Metropolis et al, 1953; Hastings, 1970), which relies on a randomized decision rule that accepts or rejects the proposed model according to their fit to the data and the prior. This algorithm samples the model space with a sampling density proportional to the unknown posterior probability density function (PDF).

The Markov chain Monte Carlo algorithm that we use is presented in Drilleau et al (2013) and Panning et al (2015). The reader is referred to these papers for further details on the practical implementation of the method. The parameterization of the V_S and $V_P - V_S$ profiles is done with Bézier points, also known as control points (Bézier, 1966, 1967). The points are interpolated with C^1 Bézier curves. The advantage of such a parameterization is that it relies on a small number parameters that do not need to be regularly spaced in depth. Similarly to Panning et al (2015), we use between 11 and 15 Bézier points to parameterize our mantle velocity models.

We test and apply this method to retrieve a synthetic martian seismic model. This model is derived from the Dreibus-Wänke mineralogy profile (Dreibus and Wänke, 1985) using the hot end-member temperature profile, to which we have added a dual-layered crust in order to test our ability to resolve mid-crustal discontinuity structure (dashed lines in fig. 4). The attenuation profile is taken from Zharkov and Gudkova (1997). The model is considered to be isotropic. In the following sections we detail and present results from the two inversions and the resulting velocity profiles. The synthetic signals used in these inversions were computed with the MINEOS package and correspond to a quake of magnitude 6.0, at 45° epicentral distance, corresponding to a moment of $10^{18.1}$ Nm. In the next section, we compare results for both a noise-free signal and a noisy signal. The noise is calculated using the complete InSight seismic noise model described in detail in Mimoun et al (2016).

In this model many possible noise sources are considered including contributors due to the mission’s instrument itself and to its thermal and magnetic sensitivities, in addition to external contributors such as the mechanical noise originating from the wind-lander interactions (Murdoch et al, 2016b) and the pressure induced ground tilt (Kenda et al, 2016; Murdoch et al, 2016a). Both signals are shown in Figure 5. Additional work has also been done analyzing coupling of wind noise through the Wind and Thermal Shield (WTS) (Teanby et al, 2016, this issue).

3.2 Inversion of group velocity dispersion diagrams: The S-wave velocity model

Using the MCMC method, we invert for the great-circle averaged group velocities of surface Rayleigh waves. Following Panning et al (2015), if we are able to record up to the 3rd orbit surface waves, the group velocity U is then

$$U = \frac{2\pi r}{R3 - R1}, \quad (2)$$

where $R1$ and $R3$ are the arrival times of the first and third orbit of Rayleigh waves, and r is the planetary radius. Note that U is independent of the event location such that the event does not need to be precisely located for this method to retrieve a 1-D velocity model. U can however depend on the azimuth of the surface wave train, as the average group velocity along the great circle linking the event and the station will depend on lateral variations, including ellipticity (Larmat et al, 2008).

Since $R3$ is not normally easily pickable, due to the dispersion of surface waves and the presence of noise, the measurements of the fundamental mode group velocities correspond to a dispersion diagram (fig. 6a for noise-free synthetic data, and fig. 6b for noisy synthetic data). These diagrams are computed (eq. 2) using the likelihood of the $R3$ arrival time in a given frequency band, as defined by the amplitude of the envelope of the seismic waveform in a series of narrow band Gaussian filters. On the plots, for a given frequency, the sum of the probability density of all the group velocities is then equal to one.

In the forward problem, we use the MINEOS software (based on work from Gilbert and Dziewoński (1975) and Woodhouse (1988)) to compute the dispersion curves for all sampled models in the 50-180 s period band. These curves are then compared to the data in figure 6. The accepted models are combined to retrieve the 1-D V_S profile PDF averaged along the great circle. The results of the inversions are shown in figures 4b and 6. As already demonstrated in Panning et al (2015), given that only the fundamental mode is considered, the surface waves sensitivity rapidly decreases below 400 km depth and the V_S distribution is not shown deeper. The V_S profile is well defined between the surface and 200 km depth, where the PDF is better constrained. The contours of the dispersion curves associated with the whole set of accepted models are plotted on top of the input dispersion diagrams (figure 6a and b). The solution

models all produce group velocity dispersion curves that match well with the input data.

The dispersion diagram that results from the noisy synthetic data (fig. 5 and 6b) shows several maxima for a given frequency, compared to the dispersion diagram from the noise-free synthetic data (fig. 6a). In figure 4b, we plot the 1σ standard deviation of the V_S distributions, for both the noise-free and noisy data (the solid and dashed orange lines, respectively). We observe that the distribution corresponding to the noisy data is shifted by approximately 0.3 km/s at depths greater than 150 km . This is explained by the higher amplitude of low frequencies in the noise spectrum (not shown here). The shift is also observed on the dispersion diagrams (fig. 6). An important result here is that the $\pm 1\sigma$ uncertainty around the median of the distribution contains the original input model down to 400 km depth, even with noisy data. We also tested the sensitivity of the results to a higher attenuation model which would decrease the signal to noise ratio. Results (not shown here) indicate that changing the attenuation profile by an order of magnitude does not significantly affect the recovered V_S distribution.

3.3 Inversion of the $V_P - V_S$ profile

Orbital imagery of the surface near the InSight lander, before and after landing, should provide precise source locations for some of the meteorite impacts recorded by the instruments. However, with no prior knowledge of the seismic velocities in the martian subsurface, the exact time of impact (t_0) will be unknown. We outline here and show an example of how we can use these signals to compute a $V_P - V_S$ differential velocity profile. This new profile can be used to retrieve the P wave velocity profile when combined with the S wave velocity profile recovered from the surface wave data.

We use a similar McMC approach as described earlier. If we know the surface location of the source exactly due to orbital imagery, then the only unknown we need in our model is the differential radial $V_P - V_S$ velocity structure between the impact and the lander. In this case we use a basic ray tracing algorithm (e.g. Shearer, 2009) to compute the differential $S - P$ travel times of the sampled models in the forward problem. We assume that the martian subsurface can be represented with a 1-D velocity model, and that a crust-mantle boundary is present. Therefore, we parameterize the model with two Bezier curves (one in the crust, and one in the mantle), separated by a discrete interface. The depth of that interface is a parameter in the inversion. We limit the range of sampled velocities by setting a minimum $V_P - V_S$ velocities of 0 km/s (i.e. P wave velocities must be larger than S wave velocities) and a maximum differential of 6 km/s , which is in line with proposed martian seismic velocity models (e.g. Dreibus and Wänke, 1985; Sohl and Spohn, 1997).

We have tested this approach using synthetic data from five impacts with epicentral distance of less than 2000 km . The model used to compute the

synthetic travel times is the same as the one used to compute the dispersion curves above (dashed lines in figure 4). The maximum depth reached by rays from the furthest event is approximately 400 *km*. The resulting $V_P - V_S$ profile is plotted in figure 4a. The plot shows a PDF of the accepted differential velocity models. The orange lines indicate the $\pm 1\sigma$ uncertainty around the median. Overall, we observe a good fit between the recovered and the original model.

One potential drawback of this approach is that it will only be sensitive to the crust-mantle boundary if there is a marked jump in differential $S - P$ velocities. If the total increase in P wave velocity is the same as the one in S wave velocity, then the depth of interface can not be recovered. In this test case, we have recovered the jump in differential velocities at the base of the crust (at around 80 *km*) but we are not as sensitive to the mid-crustal interface (near 50 *km*). As the change in relative velocity across the Moho is small, the recovered contrast is small, even though it is resolved at the correct depth. Better recovery of the Moho and internal discontinuities requires the inclusion of receiver functions as discussed in section 5.

By combining the velocity profiles from the inversion work above, we can recover a first-order P wave velocity profile (shown in figure 4c). The mean of the profile (dark blue line) is the sum of the means of the V_S and $V_P - V_S$ profiles, whereas the standard deviation ($\pm 1\sigma$ uncertainty around the mean shown by the orange lines) is the square root of the sum of the variances from both profiles. With the exception of a small depth range immediately above the unrecovered mid-crustal interface, the recovered profile matches well with the initial synthetic model within the 1σ uncertainty.

3.4 Modeling events without observations of higher orbit surface waves

In the previous section, we took advantage of particular data types that allow us to move forward without strong prior constraints on the velocity model. For higher-orbit surface waves (i.e. surface waves which propagate to the station either along the major arc between source and receiver or including multiple orbits of the planet), the known geometry of the planet allows us to constrain the velocity measurements of multiple-orbit surface waves even without an estimated location. For the impact data, the location is constrained by orbital imagery instead. However, we will also likely record many events that are smaller, but still allow us to make clear measurements of P and S arrivals and a dispersed first orbit surface wave, even if they are not big enough to record higher-orbit surface waves. For these events, we need to perform simultaneous inversions for both event and structural parameters. A Bayesian approach like the McMC method described above is once again a reasonable method for proceeding in this case.

3.4.1 Inversion using *a priori* information from mineral physics

One powerful technique to allow the development of tight constraints on velocity structure with a relatively limited initial dataset is to use Bayesian techniques informed by strong priors defined by thermodynamic mineral physics models (Khan et al, 2016). In this approach, we invert simultaneously for location and structural parameters following the approach of Khan and Connolly (2008).

As a demonstration of the potential for using this approach, we calculated synthetic seismograms for an *a priori* martian model. This model was calculated with a major element composition as defined by Dreibus and Wänke (1985) and a temperature profile equivalent to the “hot” profile of Verhoeven et al (2005) with a lithospheric thickness of 300 *km*. The mineral phase assemblages and resulting seismic velocities are determined following the approach of Khan and Connolly (2008), while the anelastic structure is defined following the approach of Nimmo and Faul (2013) with an assumed grain size of 1 *cm*.

Based on this radial model, synthetic martian seismograms for two events were calculated using the numerical wave propagation code AxiSEM (Nissen-Meyer et al, 2014), including a realistic noise model (Murdoch et al, 2015), although we used a constant Q model for computational reasons, which neglected the full frequency dependence of Q from the attenuation model of Nimmo and Faul (2013). The two events included a large $M_W 5.1$ event at 86.6° from the station and a smaller $M_W 3.8$ event at a closer distance of 27.6° .

To verify the simultaneous location and structure determination, observations of Rayleigh wave dispersion and arrival times of *P* and *S* waves were picked from the synthetic seismograms. The modeling of source and structure parameters proceeds for each event individually using a Bayesian approach equivalent to the one already described in section 3.1. Rather than having unknown parameters consisting of seismic velocities at a series of Bézier points, however, we instead treat a series of physical parameters as the unknown quantities. In this example, we treat the adiabatic potential temperature, crustal thickness, lithospheric thickness (as defined by the transition from a conductive to adiabatic temperature profile), and core radius as the unknown parameters. The composition is currently treated as fixed, but that could also be allowed to vary. Models of seismic structure are generated from these parameters following Connolly (2009), and we produce posterior PDF estimates of *P* and *S* velocity and density (fig. 7a-c). These estimates are constrained by *P* and *S* arrivals and, respectively, 3 orbits of Rayleigh waves for the large event, and the first orbit alone for the smaller event. A density model is included, but it is not directly constrained through the observations, but is instead determined by the *a priori* mineral physics modeling. In the case of the smaller event, deeper structure is also not directly constrained by seismic data, but is instead constrained by the assumed composition and thermal profile consistent with the shallower structure sampled by the event.

Using the model constraints from these “preliminary” models, we then predict arrival times for other body wave phases that propagate through the model, pick these as well and reinvert the expanded dataset in order to produce a “final” model (fig. 7d-f). In this way, we can produce estimates of martian velocity structure from single or small numbers of events with very well-resolved error estimates.

3.4.2 Inversion with minimal priors

In any Bayesian inversion, applying tight prior constraints produces lower error estimates on the final model distribution. This is extremely powerful if you have very good prior constraints, as assumed in the previous section 3.4.1. For the synthetic example, which was produced with a model consistent with the mineral physics constraints used in the inversion, relatively small amounts of data allowed for excellent estimation of the final model with relatively small error bars. However, MSS is proceeding with modeling both with and without the prior constraints set by thermodynamically self-consistent mineral physics models of structure.

There are multiple potential reasons to consider Bayesian models with more relaxed prior constraints. Using the mineral physics-based modeling implicitly includes several assumptions. It assumes a known homogenous mantle composition, or at least a range of possible compositions if that part of the model is allowed to vary as well (unlike in the previous section). It assumes the basic character of the temperature profiles are well represented by a variable thickness conductive layer matched to an adiabatic layer specified by a range of potential temperatures. Finally, it assumes the mineral phase assemblage is in thermodynamic equilibrium and that the elastic and anelastic properties of those phase assemblages are well represented by the empirical relationships tuned to laboratory experiments and observations of Earth properties.

None of these assumptions are particularly unrealistic, but there are feasible models that violate one or more of these assumptions. Models of magma ocean solidification produce compositionally stratified models early in Mars history that may resist mixing by thermal convection (e.g. Elkins-Tanton et al, 2003, 2005). Even in the absence of compositional stratification, models derived from seismic data that may sample lateral chemical heterogeneity unevenly may also be best fit by a model that is not consistent with the above assumptions. A relatively cold, conductive lithosphere may also preserve some non-equilibrium phase assemblages. The upper 200 km of the martian mantle also may not be in hydrostatic equilibrium, with possible significant thermal stresses and deviatoric stress supported by plate flexure. Topography/flexure analysis has however shown that the thermal lithosphere was shallower several billions years ago (Belleguic et al, 2005) and since there is no expectation of significant crustal thickening from volcanism in the past 3 billion years growing a depleted mantle layer, it may be reasonable to assume compositional continuity across the current thermally defined lithosphere/asthenosphere boundary.

For this reason, we also test methods to resolve structure using more limited prior constraints using only P and S body wave arrivals and observed group velocity dispersion of the first orbit Rayleigh wave between 20 and 250 seconds. Figure 8 shows an example of a Bayesian inversion of synthetic Earth data for 5 events at distances of 500, 1000, 2000, 4000, and 8000 km . While such a broad distribution of epicentral distances may be an optimistic estimate, the frequency range of measurements and small number of events are realistic for an early study, and so this serves as a demonstration of what can be done with minimal prior constraints and a small number of events with excellent data. Models are parameterized as a single layer crust of varying thickness, with a mantle made up of linear gradients and the mantle S velocity is allowed to vary within prior bounds with a width of 3 km/s varying linearly from a 3-6 km/s range at the top of the mantle to a 6-9 km/s range at the base of the mantle. Negative gradients are limited to being smaller than 0.005 km/s per km to ensure stability of the travel time calculation, but this needs to be included as low velocity zones in the mantle may be an important feature of the interior of Mars (e.g. Zheng et al, 2015). The number of layers in the mantle is allowed to vary between 2 and 11, with exploration of varying model dimensions accomplished using a type of Bayesian inversion called a transdimensional inversion (e.g. Bodin et al, 2012). In order to compare how the different prior constraints affect the final model, we generate a prior distribution simply by running the McMC inversion algorithm without application of acceptance criteria based on data misfit. The limit on negative gradients causes a prior distribution skewed to models with a gradient from minimum to maximum velocity in the mantle rather than a simple uniform distribution (fig. 8a), but after inversion with the McMC algorithm, the final estimated model PDF shows tight constraints around the true model (shown as white line in fig. 8b). Multiple events at a variety of epicentral distances were required to obtain similar constraints on the final model distribution as those based on a single event with the mineral physics prior constraints, though. Obtaining similar results from modeling with and without mineral physics prior constraints will allow us to search for possible violations of the mineral physics assumptions, or alternatively to verify that the assumptions are reasonable, permitting us to use the tighter constraints with confidence.

4 Local site characterization

While a significant focus of the InSight mission is on the structure of the deep interior, geophysical surface observations also provide a unique opportunity to characterize the shallow subsurface at the landing site as well as the crust beneath the landing site. Better characterization of the shallow site response can help in interpreting details of other seismic signals as well as giving a new constraint on geology of the landing site region. In terms of seismic observations, near-site structure can be best explored using high frequency signals as recorded by the short period SEIS-SP seismometer. We anticipate being able

to obtain information using both an active source (hammering by the nearby HP³ probe) and passive sources (analysis of surface wave amplification obtained from the ambient wavefield). These datasets will be critical since travel times of body waves recorded from distant events also have poor sensitivity to the crustal thickness and constrain only the travel time, i.e. the ratio of the crustal thickness by the seismic velocities. This has been one of the weaknesses of most of the lunar structure crustal inversions, which have provided relatively dispersed crustal thickness estimation despite comparable fits to the travel times. This emphasizes the need for alternative approaches to modeling the shallow structure at the landing site.

4.1 Analysis of HP³ hammering

The HP³ instrument will be deployed approximately 1-2 *m* from the surface placement of the SEIS instrument, and is planned to penetrate up to 5 *m* in depth to measure the heat flow coming from Mars' interior. The probe, which uses a self-penetration mechanism by an internal hammer and recoil springs, will generate thousands of seismic signals that can be used to analyze the shallow (several tens of meters) subsurface and shed new light on the mechanical properties of martian regolith (Kedar et al, 2016, this issue). The descent will progress in ~ 0.5 *m* hammering intervals, each interval taking between 0.5–4 hours, and each interval being separated by several days of thermal measurements. Each hammering interval consists of several hundred to several thousand strokes ~ 3 *s* apart, depending on the regolith properties. This repeated high frequency active source provides an opportunity to study the shallow structure at the landing site, in particular the thickness and elastic properties of the martian regolith.

As this analysis was not part of the mission threshold objectives, we face some significant challenges to take advantage of this known active source. While the geometry of the SEIS and HP³ instruments will be very well constrained, we are hampered by the lack of very high frequency sampling (sampling is limited to 100 *Hz* for both the SEIS-SP and SEIS-VBB sensors) and precise source-sensor timing synchronization, meaning we will not have exact timing of the hammer strokes. In order to better understand how we will be able to use this data, we perform a synthetic test using a simple model of a regolith layer over a half-space (table 2) to model the high frequency signal and downsample it according to the procedure used by the flight software for SEIS.

Seismograms in this model are calculated using a cartesian geometry mode summation approach (Herrmann, 2013) assuming the hammer strokes are sampled at every 1 *mm* of depth down to the full 5 *m* of penetration. These 5000 seismograms are displayed in figure 9. In this example it is assumed the mole travels vertically downward at a constant rate. In reality, the mole may deviate to some extent from the vertical path. Nevertheless, the mole depth can be calculated from precise distance and tilt measurements taken by the HP³

system. The distance the HP³ mole travels is measured to within 4 mm, and its angle to within a degree. In the high frequency output (figure 9 top), a direct P wave, a reflected P wave, and a multiple reflection (representing a wave that propagates up from the hammer and initially bounces off the surface and then the regolith interface before being recorded at the surface) are clearly visible. The relative slopes of these arrivals and their timing constrain the seismic velocity and thickness of the regolith layer. However, we need to simulate a realistic signal, which is both frequency-limited by the sampling of the data, as well as affected by the complex pulse shape of each hammering. This pulse shape has been measured using prototypes of the HP³ mole device (Kedar et al, 2016, this issue), and consists primarily of two major pulses related to the initial contact of the spring driven hammer followed by the impact of the counter-mass within the mole device a few milliseconds later. The combination of the downsampling and realistic source-time function leads to a smeared seismogram (figure 9 bottom). We can still distinguish two arrivals, but the slopes are more difficult to determine, and the reflection and multiple are smeared together. Initial work has shown that the signal can be resampled to higher frequency using sinc interpolation and picks can be made for the direct and reflected wave (Kedar et al, 2016, this issue), however further work involving data stacking and deconvolution of the hammer signal source-time function will likely be necessary for accurate recovery of regolith properties.

4.2 Surface wave ellipticity

We can also characterize the shallow structure at the landing site by analyzing the response of surface waves recorded at the site. Seismic ground motion experiences significant amplification, especially in horizontal directions, when passing through a soft soil layer, like the martian regolith. This amplification is caused by S-wave resonances in the soil column and is proportional to the impedance contrast between the soft surface layer and the more competent rock below (Takashi and Hirano, 1941; Sánchez-Sesma and Crouse, 2015). On Earth, this effect has been studied extensively as it can strongly increase earthquake damage (Borchard, 1970; Anderson et al, 1986). Similar site effects have also been observed in the Apollo lunar seismic data and correlated with the thickness of the regolith layer at the individual stations (Lammlein et al, 1974; Nakamura et al, 1975).

A popular method to assess the fundamental resonance frequency of a site is the H/V (horizontal to vertical Fourier spectral amplitude) ratio which can be quickly obtained from ambient vibration measurements (Nakamura, 1989). The H/V curves obtained on soft soils generally show a clear peak at a frequency that correlates with the fundamental resonance frequency of the site (e.g. Lachet and Bard, 1994; Lermo and Chávez-García, 1994; Malischewsky and Scherbaum, 2004). The physical interpretation of the H/V curve is still under discussion (Bonney-Claudet et al, 2006). Nakamura (2000, 2008) argues that SH wave resonances in low-velocity surface layer lead to the observed

H/V peak. However, other authors point to the frequency-dependent Rayleigh wave ellipticity as explanation, where the frequency of the minimum in vertical Rayleigh wave energy depends on velocity and thickness of low-velocity surface layer (e.g. Lachet and Bard, 1994; Lermo and Chávez-García, 1994; Fäh et al, 2001; Bonnefoy-Claudet et al, 2006). Bonnefoy-Claudet et al (2008) show for synthetic cases for a number of structural models that the H/V peak frequency provides a good estimate of the theoretical fundamental soil resonance, regardless of the contribution of different wave types to the wavefield. As these simulations also indicate that surface waves dominate the ambient vibration wavefield for moderate to high impedance contrasts between sediments and bedrock and surficial sources, we base the following analysis on the interpretation of site resonances in terms of Rayleigh wave ellipticity.

While the H/V peak frequency is thus independent of the actual wavefield composition, the peak amplitude, as confirmed by observations (e.g. Panou et al, 2005; Endrun et al, 2010; Endrun, 2011), is not. Recent terrestrial studies using ambient vibrations either aim at extracting Rayleigh waves, in which case the H/V curve provides a measure of Rayleigh wave ellipticity (Hobiger et al, 2012), or at modeling of the complete noise wavefield using diffuse field theory (e.g. Sánchez-Sesma et al, 2011; García-Jerez et al, 2013; Kawase et al, 2015; Lontsi et al, 2015). Possible sources for ambient seismic noise on Mars include the atmosphere, i.e. winds, and thermal stresses. Winds had a strong influence on the Viking data recorded by a seismometer on top of the lander (Nakamura and Anderson, 1979), and have been observed to generate Rayleigh waves propagating through the ground in terrestrial seismic data (Quiros et al, 2016). Diurnal variations in thermal stresses have been identified as the cause of frequent, weak, high-frequency events in the proximity of the Apollo stations on the Moon related to soil slumping (Duennebier and Sutton, 1974) which were used to extract Rayleigh wave group velocities via noise cross-correlation in the Apollo 17 Lunar Seismic Profiling Experiment (Larose et al, 2005). Tanimoto et al (2008) related diurnal temporal variations of these group velocities to cyclic solar heating and thermal effects on the regoliths elastic parameters. As these proposed sources interact with the surface of the planet, they will predominantly generate surface waves and single station methods can be used to extract the Rayleigh wave ellipticity from these data. These methods are either based on time-frequency analysis using a continuous wavelet transform (Fäh et al, 2001, 2009; Poggi et al, 2012), or on the random decrement technique (Hobiger et al, 2009, 2013; Bard et al, 2010). The measured ellipticity curves can then be inverted for shallow ground structure at the landing site. Scherbaum et al (2003) have shown that inversions of Rayleigh wave ellipticity alone are subject to strong trade-offs between layer velocity and thickness. Accordingly, borehole information (e.g. Arai and Tokimatsu, 2008) or surface wave dispersion (e.g. Dal Moro, 2015) are often used as additional constraints. For InSight, information on wave velocities or regolith thickness derived from the analysis of the HP³ hammering signal or from dust-devil generated Rayleigh waves could be used to *a priori* constrain the ellipticity inversion.

Here, we show an example for the inversion of a theoretical Rayleigh wave ellipticity curve calculated for a reasonable model of the shallow subsurface at the InSight landing site. Mapping of rocky ejecta craters in high-resolution orbital images and fragmentation theory based in impact crater measurements indicate a broken up regolith that is 2.4-17 *m* thick that is dominated by cohesionless sand or very low cohesion soils that grades into coarse, blocky ejecta that overlies strong, jointed bedrock (Pivarunas et al, 2015; Warner et al, 2016; Golombek et al, 2016, this issue). Regolith P- and S-wave velocities are derived from laboratory measurements on two volcanic sands (Delage et al, 2016, this issue). P-velocities for blocky ejecta, fractured and intact basalt are obtained from terrestrial field measurements on similar material (Wells et al, 1985; Vinciguerra et al, 2005).

The ellipticity curve is calculated for a model with 10 *m* regolith thickness (fig. 10a), and typical error margins from terrestrial applications are assumed. A more detailed analysis and full wavefield modeling to demonstrate the extraction of Rayleigh waves from ambient vibration measurements is presented elsewhere (Knappmeyer-Endrun et al, 2016, this issue). The H/V peak observed in the forward calculation (fig. 10a) is clearly related to the thickness of the regolith layer and the associated velocity contrast by the $\lambda/4$ rule of thumb (e.g. Malischewsky and Scherbaum, 2004). With a peak frequency of 5 *Hz*, it lies well within the frequency range covered by both the broadband and the short period seismometers. While teleseismic recordings will not be affected by site amplification around this frequency, it would increase the horizontal components' amplitudes in the study of closer events. The ellipticity peak, as well as the details of the ratio on its right and left flanks are inverted with the Conditional Neighbourhood Algorithm (Sambridge, 1999; Wathelet, 2008) as implemented in GEOPSY (Wathelet et al, 2004, www.geopsy.org). Like the Bayesian methods discussed in section 3, the method relies on random sampling of the model space, which allows us to investigate uncertainty and non-uniqueness in the inversion. The inverse model was parametrized as consisting of three layers: regolith with low velocities increasing according to a power law to a depth of 5-15 *m*, an intermediate layer 5-30 *m* thick to represent the coarse ejecta/fractured basalt, and basaltic basement with P- and S- wave velocities above 3000 *m/s* and 1500 *m/s*, respectively. Results from five inversion runs starting with different random seeds are shown (fig. 10). All models with a misfit value below 0.26 can explain the ellipticity curve within the given error bars (fig. 10b). Though the model parameterization of the inversion is considerably simpler than the actual input model which contains gradational variations between layers and two separate layers for the coarse ejecta and the fractured basalt on top of the intact material, the inversion results recover the main parameters of the model well (fig. 10c and d). While the regolith velocities are slightly overestimated, the regolith thickness estimates cluster around 10.8 *m* and 13.7 *m*, compared to an actual thickness of 10 *m*, in two distinct families of models. The difference between the two families is characterized by the mentioned depth-velocity trade-off occurring in the deeper layers. The first family, with the shallower regolith thickness,

also provides reasonable estimates for the depth to the contact between coarse ejecta and fractured basalt and the velocity of the basement, although these parameters are in general less well constrained than those in the shallow layers. A tighter constraint on the maximum regolith thickness, e.g. from analysis of the seismic recordings of HP³ signals or mapping of rocky crater ejecta, would help to distinguish between the model families, and in turn results in tighter constraints on the deeper structure from the ellipticity inversion.

5 Crustal modeling with receiver functions and surface wave ellipticity

Receiver function modeling of P-to-S (Langston, 1979) and, more recently, S-to-P (Farra and Vinnik, 2000) conversions has been a workhorse of passive seismic imaging of Earth's crust, mantle lithosphere, and transition zone structure. Receiver function modeling was also used on the Moon with seismic records originating from deep Moonquakes (Vinnik et al, 2001). In both cases, the location of the seismic source is not required when 3 axis seismic records are available. With teleseismic P and S waves of multiple marsquakes expected to be observed by InSight, receiver function modeling will yield new constraints on the internal crustal and lithospheric layering of Mars.

In this method, a free-surface transform can be used to estimate the incoming teleseismic and locally converted wavefields (Kennett, 1991) from three component data, and the incoming wavefield is deconvolved from the scattered wavefield to remove source-side complexity and yield a receiver function. The lag time and amplitude of converted waves carries information on the depth and strength of the impedance contrast that produced them; variation with back-azimuth can be used to infer dipping layers and seismic anisotropy (e.g. Kosarev et al, 1984), although these are second order constraints compared to the depth and strength of the impedance contrast, which do not depend strongly on the source distance or location. Note that the strength of the impedance contrast can be a critical additional datapoint against the non-uniqueness of solutions obtained with only differential travel times, as has been illustrated for the Moon (Lognonné et al, 2003). Because the presence of noise can destabilize deconvolution, a variety of deconvolution algorithms have been developed (e.g. Ligorria and Ammon, 1999; Park and Levin, 2000), including ones that fully quantify non-uniqueness and uncertainty associated with the deconvolution step (e.g. Kolb and Lekić, 2014), or even dispense with the need for deconvolution by probabilistically accounting for source side effects (Dettmer et al, 2015).

Relating receiver functions to structure is a notoriously non-unique problem, since they are dominantly sensitive to changes in impedance across interfaces, rather than to absolute seismic velocities (Ammon et al, 1990). Therefore, model space search approaches, especially those that do not make assumptions on the number or location of structural layers beneath the receiver, show great promise. An additional source of uncertainty in receiver function

interpretation from InSight stems from uncertainty in estimates of the ray parameter of the incoming teleseismic wavefield.

When the receiver functions are combined with complementary measurements, such as those of Rayleigh wave dispersion (Julia et al, 2000; Bodin et al, 2012) or ellipticity, receiver functions can dramatically reduce non-uniqueness of structural inferences, and yield reliable estimates of both absolute shear and compressional wave speeds. For the ellipticity measurements, we focus on a frequency band extending to lower frequencies than that used in section 4.2, and focus on measurements from Rayleigh wave recordings from marsquakes rather than the ambient wave field. While ellipticity measurements are sensitive to shallower structure than surface wave dispersion measurements at the same frequency, they have been shown to be sensitive to crustal scale velocity structure on Earth (e.g. Tanimoto and Rivera, 2008). Following the convention of Tanimoto and Rivera (2008), we take the ratio of the vertical component amplitude to the horizontal in this modeling, which is commonly termed the ZH ratio.

To simultaneously tackle these challenges of robust receiver function interpretation at Mars, we once again adopt a Bayesian approach to inversion. In this case, we use a transdimensional, hierarchical Bayesian joint inversion of receiver functions and Rayleigh wave ellipticity, which are both single-station measurements feasible with InSight. As in section 3.4.2, allowing the number of model parameters to vary in a transdimensional approach makes no prior assumptions on the number or depth of structural layers, while being inherently parsimonious and yielding an ensemble of models that can be analyzed to fully quantify uncertainty and trade-offs.

In figure 11, we show the results of such an inversion for a synthetic model (dashed black line) where we have assigned a 10% uncertainty for ZH ratio data and receiver function uncertainties 10 times larger than those obtained at a temporary broad band seismometer deployed on Earth (station M12A of the Transportable Array). The synthetic model is the same model for Mars as used in sections 3.2 and 3.3. We include 9 different receiver function inputs calculated for ray parameters ranging from 0.06-0.1 s/km , which corresponds to a distance range of 40°-90° in model A from Sohl and Spohn (1997) or 70°-90° in the synthetic model used in this section. To include information from crust and mantle lithosphere reverberations (i.e. multiples), which allow better constraints to be placed on V_P and V_S , we use receiver functions with a maximum lag time of 100 seconds following the P arrival. Separate, flexible parameterization is used for density and seismic velocity, because the expected resolution of density is low and is not shown in figure 11. No anisotropy or dipping layers are included in this test. The inclusion of multiples in the modeling procedure also increases the non-linearity of the inverse problem. We apply a simulated annealing type technique (Kirkpatrick et al, 1983) to improve the convergence of the McMC algorithm used here. We start by fitting low-pass filtered versions of the receiver functions (central frequency of 0.1Hz) together with the ZH ratio data. After every 10^5 iterations, we include higher frequencies in the receiver functions (central frequencies of 0.2Hz and 0.33Hz) and continue the

McMC with the current model. At lower frequencies, receiver functions tend to have simpler waveforms and are easier to fit, thereby reducing the chance of the McMC getting trapped at local minima. By slowly increasing the range of frequencies included in the analysis, we allow more detailed structure to be inferred from the data, while still keeping the sampling close to the global minimum. Figure 11 shows the profiles of V_P and V_S obtained after including the $0.33Hz$ center frequency receiver function together with ZH ratio data. We can see that we are able to not only recover the profile of V_S in the crust and mantle lithosphere, but also that of V_P , as well as the depths of major discontinuities (fig. 11).

If we have receiver functions recorded from several different epicentral distances (and, therefore, varying incoming ray parameters), it is possible to use receiver function data on its own to resolve major discontinuities. However, supplementing receiver functions with ZH ratio data greatly improves our ability to constrain the velocity structure. Indeed, as can be seen in the transition expectation value, which peaks at two distinct depths in figure 11, the mid-crustal discontinuity and crust-mantle boundary are clearly resolved. Constraining the crustal thickness beneath the landing site allows us to place much tighter constraints on our estimates of global crustal structure. Global scale modeling of gravity and topography variations (e.g. Neumann et al, 2004) give good constraints of the variation of crustal thickness of Mars, but do not constrain the average crustal thickness. When gravity and topography data are modeled using the assumption of isostasy, the 1-sigma uncertainties in average crustal thickness are found to lie between 33 and 81 *km* (Wieczorek and Zuber, 2004). Using seismic data from InSight to constrain the crustal thickness at the landing site, however, allows us to anchor those global models and greatly tighten our constraints on crustal thickness everywhere on Mars.

6 Observation of core and deep mantle phases

The seismic sampling of the deep interior of Mars is possible if the amplitudes of seismic phases reflected off or transmitted across the core-mantle boundary (CMB) fall above the predicted mean martian background noise of $10^{-9} m/(s^2 Hz^{1/2})$ (Murdoch et al, 2015; Mimoun et al, 2016, see fig. 12). The ray theoretically predicted amplitudes for a medium seismicity support a likely observation of P and S energy interacting with the Martian CMB for events with greater than $M_W 4.5$ ($\sim 10^{16} Nm$). For the mission duration, we would expect to record on the order of 10 events of at least this magnitude (fig. 3).

Figure 12b and c show spectral ground acceleration amplitudes of core reflected and transmitted phases on Mars for models based on the bulk composition of Dreibus and Wänke (1985) (fig. 1 and 12a) while assuming different core radii consistent with recent moment of inertia and k_2 Love number measurement (Konopliv et al, 2016; Genova et al, 2016). Amplitudes are calculated considering attenuation as well as geometric spreading and reflec-

tion/transmission coefficients at discontinuities encountered along the ray path (Aki and Richards, 2002). Core-reflected amplitudes vary over almost one order of magnitude for events very close to the receiver, and for events at 40° epicentral distance. Amplitudes for core-transmitted phases show strong variation for events close to the antipode (fig. 12b). For events with magnitudes above 10^{16} Nm , PcP, ScS, PKP as well as SKS signals are expected to lie above the lander noise (fig. 12c). Thus, seismic energy interacting with the Martian core-mantle boundary may be observable even in unfiltered and unstacked data, contrary to seismic data recorded by the Apollo missions sampling the deep interior of the Moon (e.g. Nakamura, 2005; Lognonné and Johnson, 2007; Knapmeyer, 2009).

Predicted travel-time curves for core phases on Mars are shown in fig. 13a for an event at the surface. Single station techniques already outlined for the InSight mission (Panning et al, 2015; Khan et al, 2016; Böse et al, 2016) may determine epicentral distance within an error of approximately 5% for large enough events, facilitating the determination of absolute travel-times (fig. 13a and b). With decreasing core size, core-reflected and -transmitted waves arrive at steeper angles, and thus lower ray parameters (fig. 13b). Thus, the determination of absolute travel-times as a function of ray parameter for epicentral distance ranges of 100 to 150° allows us to estimate the transfer from PcP/ PKP to Pdiff and ScS/ SKS to Sdiff, and therefore an estimation of the P and S core shadow (see Knapmeyer, 2011).

The resolution of core phases on Mars can be further improved by applying stacking techniques to account for the expected background noise and interfering seismic phases, especially due to triplications possibly caused by an analog to the Earth's mantle transition zone at depths between approximately 1000 to 1500 km . These stacking techniques are commonly applied on Earth to improve detection of seismic energy of low signal-to-noise ratio (Schweitzer et al, 2002; Deuss, 2009; Rost and Thomas, 2009; Schmerr et al, 2013) and were also used to infer the radial structure of the lunar core as well as that of an overlying partial melt layer (Weber et al, 2011; Garcia et al, 2011; Khan et al, 2014). Even if source depth and source location for any given event may have large uncertainties during a single-station mission to Mars, different phases can be distinguished by their slownesses. In principle, slowness can be directly estimated from a single arrival based on polarization, although such an estimate may have significant errors. With multiple events, however, we can improve our estimation of slowness by examining coherence of arrivals in distance and time across multiple events, although the error of this estimation will require careful error propagation from the uncertain distance determinations. Prior to the summation of the traces of individual events, signals are aligned to a reference phase, e.g. the PcP onset assuming various core radii as applied to deep moonquakes. A maximum in signal coherency corresponds to the best fitting core radius. In the case of lunar seismograms, the coherency of the stacked signals can even be further improved by applying polarization filters (Jarosch, 1977; Weber et al, 2011). Such filtering may also be useful on Mars depending on the scattering environment of the shallow martian regolith.

Core detection using seismic data with a single-station mission to Mars has a high potential for success, since ray-theoretical modeling through preliminary martian structure models such as the model by Rivoldini et al (2011) predict amplitudes above the expected lander noise (fig. 12). Determining relative PcP-P and ScS-P travel-times in the pre- or post-stacks (fig. 13) as a function of ray parameter allows for a core size estimate independent of source location, and the identification of the onset of Pdiff and Sdiff phases. Diffracted phases indicate the size of the core shadow and can be used to give an additional constraint on the core size (Oldham, 1906; Knapmeyer, 2011). This method, however, requires strong seismicity at an epicentral distance range between 100° and 150° due to the difficulty of determining a reasonably precise onset of Pdiff or Sdiff phases using data detected at a single station.

A valuable additional target for constraining the temperature and pressure state of the mantle would be sharp mantle transition zone discontinuities analogous to those on Earth interpreted as indicators of the phase transitions from olivine to wadsleyite and ringwoodite (e.g. Lay and Wallace, 1995; Deuss, 2009). However, due to different physical conditions (lower pressure and temperature) and the expected higher iron content of the martian mantle compared to the Earth's mantle, thermodynamic models constructing the phase equilibria (Khan and Connolly, 2008; Rivoldini et al, 2011) show more gradual phase transitions in the orthopyroxene ($\sim 800\text{km}$) and the olivine-wadsleyite-ringwoodite-pervoskite system ($\sim 1100\text{km}$ and $\sim 1400\text{km}$, respectively). Hence, contrary to Earth models like PREM, ray theory does not predict seismic reflections for the velocity models in figure 1. Some earlier models using slightly different composition and assumed thermal profiles (e.g. Okal and Anderson, 1978; Sohl and Spohn, 1997) show sharper transitions which can produce reflections. However, even for these models, the expected amplitude of the reflections as predicted by ray theory are significantly weaker than the core reflected phases, and so seismic phases interacting with these discontinuities are likely to be quite difficult to observe.

7 Normal modes and tides

Normal modes, or free oscillations, are the finite frequency response of a planet, and their frequencies do not depend on the excitation processes. Normal modes were therefore an early proposal as the ideal way to obtain the internal structure of Mars with a single station (e.g. Bolt and Derr, 1969), and discussed again by papers published during the design phase of Viking and Mars96 respectively (Okal and Anderson, 1978; Lognonné and Mosser, 1993). The instruments finally delivered for these two missions nevertheless lacked sufficient long period response to observe normal modes. Instruments developed since the early 90's, however, provide the necessary long period sensitivity, even if limited by thermal noise at very long period (Lognonné et al, 1996; Lognonné et al, 2000).

The excitation of normal modes by marsquakes was studied by Lognonné et al (1996) and later by Gudkova and Zharkov (2004). Both studies concluded that the observation of normal modes between 5 and 20 mHz with a noise level of $10^{-9} m/(s^2 Hz^{1/2})$ will be possible from stacked records of multiple smaller quakes with a cumulative $10^{18} Nm$ moment or from single-record analysis of the greatest quakes. This level of seismicity would be towards the upper end of reasonable expectations during the nominal mission (fig. 3), and so such observations may be possible during the InSight mission, although certainly not guaranteed. The required noise performance, though, is consistent with the expectations for the InSight VBBs during night operation. The amplitude of the continuously excited normal modes are less constrained. Kobayashi and Nishida (1998) estimated Mars' hum level to be comparable to the Earth's in amplitude of the order of 3 nanogals. Amplitudes in the range of $0.5-1 \times 10^{-9} m/(s^2 Hz^{1/2})$ are therefore expected, as on Earth. Smaller amplitudes were modeled by Lognonné and Johnson (2007), but at periods longer than 300 s . Recent simulations by Nishikawa et al. (2016) confirm amplitudes near $10^{-9} m/(s^2 Hz^{1/2})$ at 100 s .

The detection of normal modes is therefore likely during night measurements when the external wind/pressure and temperature noise are at a minimum. We therefore illustrate in this section the inversion capability of these normal modes frequencies. Normal modes have been used extensively for inversion of the Earth structure, including very early usage of Monte-Carlo techniques (e.g. Press, 1968), and have led to increasingly accurate Earth models, including PREM, one of the most widely used Earth reference models (Dziewonski and Anderson, 1981).

We illustrate here a simple inversion of fundamental mode eigenfrequency. The eigenfrequency values are estimated from the maximum of the peaks detected in the synthetic signals presented in section 3 (fig. 5). The periods of the data modeled range between 40 and 200 s (0.005 to 0.025 Hz). We consider all the frequency peaks with an amplitude higher than a moving window root mean squared (RMS) average, with window length arbitrarily set to define 61 evenly spaced intervals over the entire time series. The uncertainty on each eigenfrequency value is set to be 1/4 of the width at half the peak's amplitude. These uncertainties are dependent on the signal's length. The spacing of Mars fundamental spheroidal normal modes is about 0.2 mHz . With an 8 hour time series, a frequency resolution of 0.035 mHz is achieved, corresponding to about 1/7 of the spacing between two modes. The optimum length of record will depend on both the seismic noise and the attenuation of normal modes. The attenuation is expected to be consistent with a quality factor in the range of 100-150, based on extrapolation of the the Phobos tidal attenuation (e.g. Lognonné and Mosser, 1993).

Figure 14 shows the spectra of the noise-free signal and of the same signal with expected instrumental and environmental noises added (same noise model as discussed in section 3). Selected peaks for the inversions are also indicated. We use a similar inversion process as the one described in section 3. The MINEOS package is used to compute the eigenfrequencies of the investigated

velocity models. We favor and converge towards models that produce a larger number of corresponding eigenfrequencies (within the uncertainties ascribed). The results for inversions with noise-free and noisy data are shown in Figure 15a and 15b, respectively. In both cases, the input model (in dashed lines) is retrieved down to ~ 200 km depth. The V_S model distribution is not as well defined for the noisy data, due to the presence of frequencies, not related to the event, introduced by the noise. Further work will be done to improve the detection of eigenfrequencies within the spectrum and the misfit function, but with these two examples we show the potential of using normal modes to explore the martian crust and upper mantle.

Several future improvements are expected, such as those leading to an identification of the angular orders of the peaks (not used in this example) or those improving the quality of the mode's signal to noise ratio with multiple taper methods (e.g. Park et al, 1987). Neither the seismic moment of the largest expected quake nor the strength of the hum excitations will be large enough, however, to excite in a detectable way the lowest angular order normal modes which are sensitive to the deep structure of the planet, including the core. The inversion of the Love number, through the gravimetric factor – a function of the h and k Love numbers that is defined as the ratio between tidal gravity variations of the planet compared with those expected for a rigid body (e.g. Dehant and Ducarme, 1987) – will therefore put important additional constraints on the core size, in addition to those provided by SEIS for the core phases described in section 6 and by RISE (which will determine very precise orbital parameters through radio tracking of the lander), through the measurement of Mars' nutation. These can be combined with the Love number k_2 , already measured from precise tracking data (e.g. Konopliv et al, 2016; Genova et al, 2016). We illustrate the complementarity of these constraints with figure 16, where both the ScS travel times (at 1 Hz), the gravimetric factors (at Phobos tidal period) and the k_2 Love numbers (at solar tidal period) are shown for the models DW and EH45, either hot or cold. A power law dependence for Q, comparable to Earth physical dispersion models (e.g. Lekić et al, 2009) and used for Mars by Lognonné and Mosser (1993) and Zharkov and Gudkova (1997), has been used with $\alpha \sim 0.05$, which predicts Q factors of 86 and 90 for Solar and Phobos tide and shear Q in the mantle of 143 at 1 Hz. The alpha value was chosen in this case so the Phobos Q is in the range of observations (e.g. Bills et al, 2005). This relationship predicts physical dispersion that decreases the shear modulus by about 3% between 1 Hz and solar tide, while an increase of about 0.5% in the Love number is expected between Phobos and Solar tides. This model for attenuation is, however, not unique, and other dispersion models can be used, such as those proposed by Jackson and Faul (2010). For SEIS, the largest constraint will be related to the absolute calibration of the seismometer gravity output, which we require to be $\pm 0.35\%$, in order to contain the core size estimate to $\pm 0.5\%$. All these data will finally be used for more complete inversion of the deep interior, which will be important in decreasing trade-offs between core size and possible low shear modulus structure in the lower mantle.

8 Discussion and conclusions

The MSS plans on developing models covering a variety of depth ranges, from very near surface techniques to look at regolith thickness all the way to normal mode observations sensitive to averages of global structure from the surface to the core. In the process, we will also use a variety of seismic data types, as well as including results from heat flow measurements of HP³ and core radius and state from the RISE radio science.

8.1 Strengths of Bayesian modeling

While initial work may focus separately on using particular data types to look at particular aspects of the interior, one of the critical aims of our modeling effort is to use Bayesian approaches that allow us to accommodate different data types or models inferred from them in a very natural framework. This can be done in two different ways: joint inversions of multiple data types, and including modeling results from particular data types as prior constraints in Bayesian modeling.

It is quite natural to do joint inversions of multiple data types with Bayesian approaches. Relative data weighting, which is a persistent challenge in joint inversions with data types that may not have well defined data variance estimates, can even be accommodated with hierarchical approaches (e.g. Bodin et al, 2012) which treat data variance as an additional uncertain parameter, thus allowing us to quantify additional uncertainties arising from varying data weighting schemes. However, joint inversions may not always be practical. For example, normal mode constraints and HP³ hammering signals operate on such different length scales that attempting to model both simultaneously is not useful. However, modeling results can be used to constrain the prior probabilities that govern Bayesian inversions. For example, crustal thickness constraints from receiver functions, and core radius constraints from RISE data can be used to define the a priori estimates that go into a Bayesian inversion of body wave and surface wave observations for mantle structure. As another example, HP³ heat flow measurements can be used to define tighter prior constraints on the input thermal profile for the modeling including mineral physics constraints as in section 3.4.1.

8.2 Lateral variations

The seismic simulations and modeling discussed so far consider radially symmetric models. The effect of Mars topography and crustal thickness variations on long-period surface waves (periods longer than 80 s) were previously investigated by Larmat et al (2008) where up to 6 s time shifts and within about 4% amplitude variations were reported due to the crustal dichotomy between the northern and southern hemispheres. To better model what we may expect

from the InSight mission, we performed higher-resolution numerical simulations to examine the effect of 3D variations on shorter-period global ($>\sim 10$ s) and regional ($>\sim 2$ s) seismic waves (Bozdağ et al, 2016). For global simulations, we use the open source spectral-element solver SPEC-FEM3D-GLOBE, originally developed by Komatitsch and Tromp (2002a,b), which accommodates 3D elastic and anelastic seismic models, as well as effects due to topography, gravity, rotation, and ellipticity. We first implemented a 1D Mars model constructed by Sohl and Spohn (1997) with a 110 km thick crust and a 1D Q -profile adapted from the 1D Earth model PREM (Dziewonski and Anderson, 1981). We then included the effects of ellipticity, gravity and rotation (Williams, 2016). Using 3D crustal thickness variations determined from gravity measurements by Wieczorek and Zuber (2004) and high-resolution topography from the Mars Orbiter Laser Altimeter (MOLA), we investigated effects of surface topography and the dichotomy in crustal thickness between Mars' southern and northern hemispheres on seismic waves with periods down to ~ 10 s. To assess the stability and robustness of numerical simulations, we benchmarked SPEC-FEM3D-GLOBE seismograms computed for the 1D reference model (Sohl and Spohn, 1997) to those from the 2.5D axisymmetric spectral-element solver AxiSEM (Nissen-Meyer et al, 2014) down to 10 s. Furthermore, we demonstrated the 3D crustal effects, not only thickness variations but also 3D wavespeed variations within the crust, on regional waveforms using the regional spectral-element solver SES3D (Fichtner et al, 2009), which uses regular grids on spherical coordinates, down to 2 s. Our initial experiments show that the numerical tools are ready for examining various realistic wave propagation scenarios on Mars using different seismic models as well as sources.

As our amount of data increases, we may be able to start using events recorded from different source regions to constrain how much variation in crust and mantle structure we actually have on Mars. Determining the degree 2 structure of the planet will require at least 5 quakes with R1 and R3 measurements. Using these measurements, we can constrain great-circle average structure which depends mostly on the spherical harmonic degree 2 structure and has no sensitivity to odd degrees. Such a goal is likely within 1-2 martian years. The determination of the degree 1 and 3 of the planet will, however, be more challenging, as they will require the use of R1, R2 and R3 which can provide the origin time, location and group velocity. Relative comparison of the R1 and R2 dispersion of surface waves can nevertheless allow for determination of the differences in crustal and lithosphere structure between the north and south hemisphere.

8.3 Interaction with Marsquake Service

The two operational services of the SEIS instrument team (MSS and MQS) are necessarily closely related. Accurate structure models improve quake location, while accurate quake location is essential for better resolution of structure.

Throughout the mission, engagement between these services will be essential. Some of the techniques described here are actually simultaneous inversions for structure and source parameters, and so do not fit easily into a silo concept where separate researchers work only on one side of the problem. Communication and crossover between the management and products of both of these groups will foster the best results in delivering the desired science outcomes from the InSight mission.

8.4 Planetary Data System deliverables

The SEIS team has the responsibility to deliver several products to the final, official Planetary Data System (PDS) archive for the InSight mission. These include calibration and instrument transfer function information prior to landing and after calibration on the martian surface, and raw and calibrated continuous and event-specific data from both the broadband and short period instruments as well as engineering temperature on a quarterly basis. Finally, SEIS is responsible for delivering a set of geophysical structure and seismic velocity models (from MSS) and a seismic source catalog (from MQS) 5 months after the end of mission.

While the PDS archive is not required until after the end of the mission, both MSS and MQS will be making products available to the community with frequent updates whenever new data becomes available. In particular, data will be archived in the IRIS (Incorporated Research Institutions for Seismology) Data Management Center (DMC) soon after it is verified for quality. This will allow the final archived version to represent a mature set of models and structure catalogs based on evolving data and improved methodologies through the course of the mission.

9 Conclusions

Based on estimates of seismic activity levels on Mars, we anticipate recovery of seismic data capable of resolving structure on a wide variety of length scales. Initial models will be based on body wave and surface wave data which does not rely strongly on *a priori* knowledge of structure, as well as approaches that allow for simultaneous inversion of structure and source parameters. Shallow site response can be analyzed with signals from the HP³ hammering as well as high frequency measurements of surface wave ellipticity. Crustal scale structure can be resolved with receiver functions and lower frequency measurements of surface wave ellipticity. Ray theory modeling suggests that we should be able to observe core-interacting phases to better resolve properties of the martian core. Normal modes observations are feasible and can constrain globally averaged structure. Data from a single seismic station on Mars by the InSight lander will enable us to greatly improve our understanding of the interior structure of the planet.

Acknowledgements Research described in this paper was partially done by the InSight Project, Jet Propulsion Laboratory, California Institute of Technology, under a contract with the National Aeronautics and Space Administration. This work has been supported by CNES for all French institutions' co-authors. S.H, J.B.G and the IPGP, ISAE and Univ. Nantes teams have been also supported by ANR (ANR-14-CE36-0012 "Seismology on Mars") and PL by Institut Universitaire de France. The Bayesian inversions of section 3 were performed using HPC resources of CINES (Centre Informatique National de l'Enseignement Supérieur) under the allocation 2015047341 made by GENCI (Grand Equipement National de Calcul Intensif). A.K. was supported by grants from the Swiss National Science Foundation (SNF-ANR project 157133 "Seismology on Mars") and from the Swiss National Supercomputing Centre (CSCS) under project ID s628. N.T. and J.W. were supported by funding from the U.K. Space Agency. The open source spectral-element software packages SPECFEM3D GLOBE and AxiSEM are freely available via the Computational Infrastructure for Geodynamics (CIG; geodynamics.org). For SPECFEM3D GLOBE simulations computational resources were provided by the Princeton Institute for Computational Science & Engineering (PICSciE). This paper is InSight Contribution Number 22.

References

- Aki K, Richards PG (2002) *Quantitative Seismology*, second edition edn. University Science Books, Sausalito, CA
- Ammon CJ, Randall GE, Zandt G (1990) On the nonuniqueness of receiver function inversions. *J Geophys Res* 95(B10):15,303–15,318
- Anderson D, Miller W, Latham G, Nakamura Y, Toksöz M (1977) Seismology on Mars. *J Geophys Res* 82:4524–4546
- Anderson J, Bodin P, Brune J, Prince J, Singh S, Quaas R, Onate M (1986) Strong ground motion from the Michoacan, Mexico, earthquake. *Science* 233:1043–1049
- Arai H, Tokimatsu K (2008) Three-dimensional Vs profiling using microtremors in Kushiro, Japan. *Earthq Eng Struct Dyn* 37:845,859, DOI 10.1002/eqe.788
- Banerdt W, Smrekar S, Lognonné P, Spohn T, Asmar S, Banfield D, Boschi L, Christensen U, Dehant V, Folkner W, Giardini D, Goetze W, Golombek M, Grott M, Hudson T, Johnson C, Kargl G, Kobayashi N, Maki J, Mimoun D, Mocquet A, Morgan P, Panning M, Pike W, Tromp J, van Zoest T, Weber R, Wiczorek M, Garcia R, Hurst K (2013) InSight: A Discovery mission to explore the interior of Mars. In: 44th Lunar and Planetary Science Conference, Lunar and Planetary Inst., Houston, TX, p Abstract #1915, URL <http://www.lpi.usra.edu/meetings/lpsc2013/pdf/1915.pdf>
- Bard PY, Cadet H, Endrun B, Hobiger M, Renalier F, Theodulidis N, Ohrnberger M, Fäh D, Sabetta F, Teves-Costa P, Duval AM, Cornou C, Guilier B, Wathelet M, Savvaidis A, Köhler A, Burjanek J, Poggi V, Gassner-Stamm G, Havenith HB, Hailemikael S, Almeida J, Rodrigues I, Veludo I, Lacave C, Thomassin S, Kristekova M (2010) From non-invasive site characterization to site amplification: Recent advances in the use of ambient vibration measurements. In: Garevski M, Ansal A (eds) *Earthquake Engineering in Europe*, Springer Science + Business Media B.V., Volume 17 of Geotechnical, Geological, and Earthquake Engineering, chap 5, pp 105–123

- Belleguic V, Lognonné P, Wieczorek M (2005) Constraints on the Martian lithosphere from gravity and topography data. *J Geophys Res* 110(E11):E11,005, DOI 10.1029/2005JE002437
- Bézier P (1966) Définition numérique des courbes et surfaces I. *Automatisme* 11:625–632
- Bézier P (1967) Définition numérique des courbes et surfaces II. *Automatisme* 12:17–21
- Bills BG, Neumann A, Smith DE, Zuber MT (2005) Improved estimate of tidal dissipation within Mars from MOLA observations of the shadow of Phobos. *J Geophys Res* 110:E07,004, DOI 10.1029/2004JE002376
- Bodin T, Sambridge M, Tkalčić H, Arroucau P, Gallagher K, Rawlinson N (2012) Transdimensional inversion of receiver functions and surface wave dispersion. *J Geophys Res* 117:B02,301, DOI 10.1029/2011JB008560
- Bolt BA, Derr JS (1969) Free bodily vibrations of the terrestrial planets. *Vistas in Astronomy* 11:69–102
- Bonnefoy-Claudet S, Cornou C, Bard PY, Cotton F, Moczo P, Kristek J, Fäh D (2006) H/V ratio: a tool for site effects evaluation. Results from 1-D noise simulations. *Geophys J Int* 167:827–837, DOI 10.1111/j.1365-246X.2006.03154.x
- Bonnefoy-Claudet S, Köhler A, Cornou C, Wathelet M, Bard PY (2008) Effects of Love waves on microtremor H/V ration. *Bull Seism Soc Amer* 98:288–300, DOI 10.1785/0120070063
- Borchard R (1970) Effects of local geology on ground motion near San Francisco Bay. *Bull Seism Soc Amer* 60:29–61
- Böse M, Clinton JF, Ceylan S, Euchner F, van Driel M, Khan A, Giardini D, Lognonné P, Banerdt WB (2016) A probabilistic framework for single-station location of seismicity on Earth and Mars. *Phys Earth Planet Int* DOI 10.1016/j.pepi/2016.11.003, in press
- Bozdağ E, Ruan Y, Mettetz N, Khan A, Leng K, van Driel M, Larmat C, Giardini D, Tromp J, Lognonné P, Banerdt WB (2016) Simulations of seismic wave propagation on Mars. *Space Sci Rev* this volume
- Burr DM, Grier JA, McEwen AS, Keszthelyi LP (2002) Repeated aqueous flooding from the Cerberus Fossae: Evidence for very recently extant, deep groundwater on Mars. *Icarus* 159:53–73, DOI 10.1006/icar.2002.6921
- Chenet H, Lognonné P, Wieczorek M, Mizutani H (2006) Lateral variations of lunar crustal thickness from the apollo seismic data set. *Earth Planet Sci Lett* 243:1–14
- Connolly JAD (2005) Computation of phase equilibria by linear programming: A tool for geodynamic modeling and its application to subduction zone decarbonation. *Earth Planet Sci Let* 236:524–541
- Connolly JAD (2009) The geodynamic equation of state: What and how. *Geochem Geophys Geosyst* 10(10):Q10,014, DOI 10.1029/2009GC002540
- Dal Moro G (2015) Joint analysis of Rayleigh-wave dispersion and HVSR of lunar seismic data from the Apollo 14 and 16 sites. *Icarus* 254:338–349, DOI 10.1016/j.icarus.2015.03.017

- Darwin GH (1882) A numerical estimate of the rigidity of the Earth. *Nature* 27:22–23, DOI 10.1038/027022b0
- Daubar IJ, McEwen AS, Byrne S, Kennedy MR, Ivanov B (2013) The current martian cratering rate. *Icarus* 225:506–516
- Davis PM (1993) Meteoroid impacts as seismic sources on Mars. *Icarus* 105:469–478
- Dehant V, Ducarme B (1987) Comparison between the theoretical and observed tidal gravimetric factors. *Phys Earth Planet Int* 49:192–212
- Delage P, Karakostas F, Dhemaied A, Belmokhtar M, De Laure D, Dupla JC, Cui YJ (2016) An investigation of the geotechnical properties of some Martian regolith simulants with respect to the surface properties of the InSight mission landing site. *Space Sci Rev* this volume
- Dettmer J, Dosso SE, Bodin T, Stipčević J, Cummins PR (2015) Direct-seismogram inversion for receiver-side structure with uncertain source–time functions. *Geophys J Int* 203(2):1373–1387
- Deuss A (2009) Global observations of mantle discontinuities using SS and PP precursors. *Surveys Geophys* 30:301–326
- Dreibus G, Wänke H (1985) Mars: a volatile rich planet. *Meteoritics* 20:367–382
- Drilleau M, Beucler E, Mocquet A, Verhoeven O, Moebs G, Burgos G, Montagner JP, Vacher P (2013) A Bayesian approach to infer radial models of temperature and anisotropy in the transition zone from surface wave dispersion curves. *Geophys J Int* 195:1165–1183
- Duennebieer F, Sutton GH (1974) Thermal moonquakes. *J Geophys Res* 79:4351–4363
- Dziewonski A, Anderson D (1981) Preliminary Reference Earth Model. *Phys Earth Planet Inter* 25:297–356
- Elkins-Tanton LT, Parmentier EM, Hess PC (2003) Magma ocean fractional crystallization and cumulate overturn in terrestrial planets: Implications for Mars. *Meteoritics and Planet Sci* 38(12):1753–1771, DOI 10.1111/j.1945-5100.2003.tb00013.x
- Elkins-Tanton LT, Zaranek SE, Parmentier EM, Hess PC (2005) Early magnetic field and magmatic activity on Mars from magma ocean cumulate overturn. *Earth Planet Sci Let* 236:1–12
- Endrun B (2011) Love wave contribution to the ambient vibration H/V amplitude peak observed with array measurements. *J Seism* 15:443–472, DOI 10.1007/s10950-010-9191-x
- Endrun B, Ohrnberger M, Savvaidis A (2010) On the repeatability and consistency of ambient vibration array measurements. *Bull Earthq Eng* 8:535–570, DOI 10.1007/s10518-009-9159-9
- Fäh D, Kind F, Giardini D (2001) A theoretical investigation of average H/V ratios. *Geophys J Int* 145:535–549
- Fäh D, Wathelet M, Kristekova M, Havenith H, Endrun B, Stamm G, Poggi V, Burjanek J, Cornou C (2009) Using ellipticity information for site characterisation. NERIES JRA4 ”Geotechnical Site Characterisation”, task B2, final report, EC project number: 026130

- Farra V, Vinnik L (2000) Upper mantle stratification by P and S receiver functions. *Geophys J Int* 141:699–712
- Fichtner A, Kennett BLN, Igel H, Bunge HP (2009) Full seismic waveform tomography for upper-mantle structure in the Australasian region using adjoint methods. *Geophys J Int* 179, DOI 10.1111/j.1365-246X.2009.04368.x
- Folkner WM, Asmar SW, Dehant V, Warwick RW (2012) The rotation and interior structure experiment (RISE) for the InSight mission to Mars. In: 43rd Lunar and Planetary Science Conference, Lunar and Planetary Inst., Houston, TX, p Abstract #1721, URL <http://www.lpi.usra.edu/meetings/lpsc2012/pdf/1721.pdf>
- Gagnepain-Beyneix J, Lognonné P, Chenet H, Lombardi D, Spohn T (2006) A seismic model of the lunar mantle and constraints on temperature and mineralogy. *Phys Earth Planet Inter* 159:140–166
- García R, Gagnepain-Beyneix J, Chevrot S, Lognonné P (2011) Very preliminary reference Moon model. *Phys Earth Planet Inter* 188:96–113
- García-Jerez A, Luzón F, Sánchez-Sesma FJ, Lunedei E, Albarello D, Santoyo MA, Almendros J (2013) Diffuse elastic wavefield within a simple crustal model. Some consequences for low and high frequencies. *J Geophys Res* 118:5577–5595, DOI 10.1002/2013JB010107
- Genova A, Goosens S, Lemoine FG, Mazarico E, Neumann GA, Smith DE, Zuber MT (2016) Seasonal and static gravity field of Mars from MGS, Mars Odyssey and MRO radio science. *Icarus* 272:228–245, DOI 10.1016/j.icarus.2016.02.050
- Gilbert F, Dziewoński A (1975) An application of normal mode theory to the retrieval of structural parameters and source mechanisms from seismic spectra. *Philos Trans R Soc London A* 278:187–269
- Golombek M (2002) A revision of Mars seismicity from surface faulting. In: 33rd Lunar and Planetary Science Conference, Lunar and Planetary Inst., Houston, TX, p Abstract #1244
- Golombek M, Banerdt W, Tanaka K, Tralli D (1992) A prediction of Mars seismicity from surface faulting. *Science* 258:979–981
- Golombek MP (1994) Constraints on the largest marsquake. In: 25th Lunar and Planetary Science Conference, pp 441–442
- Golombek MP, Kipp D, Warner N, Daubar IJ, Fergason R, Kirk R, Beyer R, Huertas A, Piqueux S, Putzig N, Campbell BA, Morgan G, Charalambous C, Pike WT, Gwinner K, Calef F, Ashley J, Kass D, Mischna M, Bloom C, Wigton N, Schwartz C, Gengl H, Redmond L, Sweeney J, Sklyanskiy E, Lisano M, Benardino J, Smrekar S, Banerdt WB (2016) Selection of the InSight landing site. *Space Sci Rev* this volume
- Gudkova T, Zharkov V (2004) Mars: interior structure and excitation of free oscillations. *Phys Earth Planet Inter* 142:1–22
- Gudkova T, Lognonné P, Miljković K, Gagnepain-Beyneix J (2015) Impact cutoff frequency – momentum scaling law inverted from Apollo seismic data. *Earth Planet Sci Let* 427:57–65, DOI 10.1016/j.epsl.2015.06.037
- Hanks TC, Boore DM (1984) Moment-magnitude relations in theory and practice. *J Geophys Res* B89:6229–6235

- Hartmann WK (2005) Martian cratering 8: Isochron refinement and the chronology of Mars. *Icarus* 174:294–320
- Hastings W (1970) Monte Carlo sampling methods using Markov chains and their applications. *Biometrika* 57:97–109
- Herrmann RB (2013) Computer programs in seismology: An evolving tool for instruction and research. *Seis Res Lett* 84:1081–1088, DOI 10.1785/0220110096
- Hobiger M, Bard PY, Cornou C, Le Bihan N (2009) Single station determination of Rayleigh wave ellipticity by using the random decrement technique (RayDec). *Geophys Res Lett* 36:L14,303, DOI 10.1029/2009GL038863
- Hobiger M, Le Bihan N, Cornou C, Bard PY (2012) Multicomponent signal processing for Rayleigh wave ellipticity estimation: Application to seismic hazard assessment. *IEEE Signal Proc Mag* 29:29–39, DOI 10.1109/MSP.2012.2184969
- Hobiger M, Cornou C, Wathelet M, Di Giulio G, Knapmeyer-Endrun B, Renalier F, Bard PY, Savvaidis A, Hailemichael S, Le Bihan N, Ohrnberger M, Theodoulidis N (2013) Ground structure imaging by inversions of Rayleigh wave ellipticity: sensitivity analysis and application to European strong-motion sites. *Geophys J Int* 192:207–229, DOI 10.1093/gji/ggs005
- Jackson I, Faul UH (2010) Grainsize-sensitive viscoelastic relaxation in olivine: Towards a robust laboratory-based model for seismological application. *Phys Earth Planet Int* 183:151–163, DOI 10.1016/j.pepi.2010.09.005
- Jaeger WL, Keszthelyi LP, McEwen AS, Dundas CM, Russell PS (2007) Athabasca Valles, Mars: A lava-draped channel system. *Science* 317:1709–1711, DOI 10.1126/science.1143315
- Jarosch HS (1977) The use of surface reflections in lunar seismograms. *Bull Seism Soc Am* 67(6):1647–1659
- Julia J, Ammon CJ, Herrmann RB, Correig AM (2000) Joint inversion of receiver function and surface wave dispersion observations. *Geophys J Int* 143(1):99–112
- Kawase H, Matsushima S, Satoh T, Sánchez-Sesma FJ (2015) Applicability of theoretical horizontal-to-vertical ratio of microtremors based on the diffuse field concept to previously observed data. *Bull Seism Soc Am* 105, DOI 10.1785/0120150134
- Kedar S, Andrade J, Banerdt WB, Delage P, Golombek M, Grott M, Hudson T, Kiely A, Knapmeyer M, Knapmeyer-Endrun B, Krause C, Kawamura T, Lognonné P, Pike WT, Ruan Y, Teanby N, Tromp J, Wookey J (2016) Analysis of regolith properties using seismic signals generated by InSight’s HP³ penetrator. *Space Sci Rev* this volume
- Kenda B, Lognonné P, Spiga A, Kawamura T, Kedar S, Banerdt WB, Lorenz RD (2016) Modeling of ground deformation and shallow surface waves generated by Martian dust devils and perspectives for near-surface structure inversion. *Space Sci Rev* this volume
- Kennett BLN (1991) The removal of free surface interactions from three component seismograms. *Geophys J Int* 104(1):153–163

- Khan A, Connolly J (2008) Constraining the composition and thermal state of Mars from inversion of geophysical data. *J Geophys Res* 113:E07,003, DOI 10.1029/2007JE002996
- Khan A, Mosegaard K (2002) An inquiry into the lunar interior: A nonlinear inversion of the Apollo lunar seismic data. *J Geophys Res* 107:5036, DOI 10.1029/2001JE001658
- Khan A, Mosegaard K, Rasmussen KL (2000) A new seismic velocity model for the Moon from a Monte Carlo inversion of the Apollo lunar seismic data. *Geophys Res Lett* 27:1591
- Khan A, Connolly J, Maclennan J, Mosegaard K (2007) Joint inversion of seismic and gravity data for lunar composition and thermal state. *Geophys J Int* 168:243–258
- Khan A, Boschi L, Connolly A (2009) On mantle chemical and thermal heterogeneities and anisotropy as mapped by inversion of global surface wave data. *J Geophys Res* 114:B09,305, DOI 10.1029/2009JB006399
- Khan A, Zunino A, Deschamps F (2013) Upper mantle compositional variations and discontinuity topography imaged beneath Australia from bayesian inversion of surface-wave phase velocities and thermochemical modeling. *J Geophys Res* 116, DOI 10.1002/jgrb.50304
- Khan A, Connolly JAD, Pommier A, Noir J (2014) Geophysical evidence for melt in the deep lunar interior and implications for lunar evolution. *J Geophys Res* 119:2197–2221, DOI 10.1002/2014JE004661
- Khan A, van Driel M, Böse M, Giardini D, Ceylan S, Yan J, Clinton J, Euchner F, Lognonné P, Murdoch N, Mimoun D, Panning MP, Knapmeyer M, Banerdt WB (2016) Single-station and single-event marsquake location and inversion for structure using synthetic Martian waveforms. *Phys Earth Planet Int* 258:28–42, DOI 10.1016/j.pepi.2016.05.017
- Kirkpatrick S, Gelatt CD, Vecchi MP (1983) Optimization by simulated annealing. *Science* 220:671–680, DOI 10.1126/science.220.4598.671
- Knapmeyer M (2009) Planetary seismology. In: Trümper JE (ed) *Solar System, Landolt-Börnstein - Group VI Astronomy and Astrophysics*, vol 4B, Springer, chap 4.2.3.3, pp 282–322
- Knapmeyer M (2011) Planetary core size: A seismological approach. *Plan & Space Sci* 59(10):1062–1068
- Knapmeyer M, Oberst J, Hauber E, Wählisch M, Deuchler C, Wagner R (2006) Working models for spatial distribution and level of Mars' seismicity. *J Geophys Res* 111:E11,006, DOI 10.1029/2006JE002708
- Knapmeyer-Endrun B, Golombek MP, Ohrnberger M (2016) Rayleigh wave ellipticity modeling and inversion for shallow structure at the proposed In-Sight landing site in Elysium Planitia, Mars. *Space Sci Rev* this volume, DOI 10.1007/s11214-016-0300-1
- Kobayashi N, Nishida K (1998) Continuous excitation of planetary free oscillations by atmospheric disturbances. *Nature* 395:357–360
- Kolb J, Lekić V (2014) Receiver function deconvolution using transdimensional hierarchical Bayesian inference. *Geophys J Int* 197(3):1719–1735, DOI 10.1093/gji/ggu079

- Komatitsch D, Tromp J (2002a) Spectral-element simulations of global seismic wave propagation – I. Validation. *Geophys J Int* 149:390–412, DOI 10.1046/j.1365-246X.2002.01653.x
- Komatitsch D, Tromp J (2002b) Spectral-element simulations of global seismic wave propagation – II. 3-D models, oceans, rotation, self-gravitation. *Geophys J Int* 150:303–318, DOI 10.1046/j.1365-246X.2002.01716.x
- Konopliv AS, Park RS, Folkner WM (2016) An improved JPL Mars gravity field and orientation from Mars orbiter and lander tracking data. *Icarus* 274:253–260, DOI 10.1016/j.icarus.2016.02.052
- Kosarev GL, Makeyeva LI, Vinnik L (1984) Anisotropy of the mantle inferred from observations of P to S converted waves. *Geophys J R Astr Soc* 76:209–220
- Lachet C, Bard PY (1994) Numerical and theoretical investigations on the possibilities and limitations of Nakamura’s technique. *J Phys Earth* 42:377–397
- Lammlein D, Latham G, Dorman J, Nakamura Y, Ewing M (1974) Lunar seismicity, structure and tectonics. *Rev Geophys Space Phys* 12:1–21
- Langston CA (1979) Structure under Mount Rainier, Washington, inferred from teleseismic body waves. *J Geophys Res* 84(B9):4749–4762
- Larmat C, Montagner JP, Capdeville Y, Banerdt W, Lognonné P, Vilotte JP (2008) Numerical assessment of the effects of topography and crustal thickness on Martian seismograms using a coupled modal solution–spectral element method. *Icarus* 196(1):78–89
- Larose E, Khan A, Nakamura Y, Campillo M (2005) Lunar subsurface investigated from correlation of seismic noise. *Geophys Res Lett* 32:L16,201, DOI 10.1029/2005GL023518
- Lay T, Wallace T (1995) *Modern Global Seismology*. Academic Press
- Lekić V, Matas J, Panning MP, Romanowicz BA (2009) Measurement and implications of frequency dependence of attenuation. *Earth Planet Sci Lett* 282:285–293, DOI 10.1016/j.epsl.2009.03.030
- Lermo J, Chávez-García F (1994) Are microtremors useful in site response evaluation? *Bull Seism Soc Amer* 84:1350–1364
- Ligorria JP, Ammon CJ (1999) Iterative deconvolution and receiver-function estimation. *Bull Seism Soc Am* 89(5):1395–1400
- Linkin V, Harri AM, Lipatov A, Belostotskaja K, Derbunovich B, Ekonomov A, Khloustova L, Kremnev R, Makarov V, Martinov B, Nenarokov D, Prostov M, Pustovalov A, Shustko G, Järvinen I, Kivilinna H, Korpela S, Kumpulainen K, Lehto A, Pellinen R, Pirjola R, Riihelä P, Salminen A, Schmidt W, Siili T, Blamont J, Carpentier T, Debus A, Hua CT, Karczewski JF, Laplace H, Levacher P, Lognonné P, Malique C, Menvielle M, Mouli G, Pommereau JP, Quotb K, Runavot J, Vienne D, Grunthaler F, Kuhnke F, Musmann G, Rieder R, Wänke H, Economou T, Herring M, Lane A, McKay CP (1998) A sophisticated lander for scientific exploration of Mars: scientific objectives and implementation of the Mars-96 Small Station. *Planet Space Sci* 46:717–737, DOI 10.1016/S0032-0633(98)00008-7

- Lodders K, Fegley B (1997) An oxygen isotope model for the composition of Mars. *Icarus* 126:373–394
- Lognonné P, Johnson C (2007) Planetary seismology. In: Schubert G (ed) *Treatise on Geophysics*, vol 10, Elsevier, Amsterdam, pp 69–122
- Lognonné P, Johnson CL (2015) Planetary seismology. In: Schubert G (ed) *Treatise on Geophysics*, vol 10, 2nd edn, Elsevier, Oxford, pp 65–120
- Lognonné P, Mosser B (1993) Planetary seismology. *Surveys Geophys* 14:239–302
- Lognonné P, Pike WT (2015) Planetary seismometry. In: Tong VCH, Garcia R (eds) *Extraterrestrial Seismology*, Cambridge Univ. Press, Cambridge, U.K., chap 3, pp 36–48, DOI 10.1017/CBO9781107300668.006
- Lognonné P, Beyneix JG, Banerdt WB, Cacho S, Karczewski JF, Morand M (1996) Ultra broad band seismology on InterMarsNet. *Planet Space Sci* 44:1237, DOI 10.1016/S0032-0633(96)00083-9
- Lognonné P, Clévéde E, Kanamori H (1998) Computation of seismograms and atmospheric oscillations by normal-mode summation for a spherical earth model with realistic atmosphere. *Geophys J Int* 135:388–406
- Lognonné P, Giardini D, Banerdt W, Gagnepain-Beyneix J, Mocquet A, Spohn T, Karczewski J, Schibler P, Cacho S, Pike W, Cavoit C, Desautez A, Favède M, Gabsi T, Simoulin L, Striebig N, Campillo M, Deschamp A, Hinderer J, Lévêque J, Montagner JP, Rivéra L, Benz W, Breuer D, Defraigne P, Dehant V, Fujimura A, Mizutani H, Oberst J (2000) The NetLander very broad band seismometer. *Planet Space Sci* 48:1289–1302
- Lognonné P, Gagnepain-Beyneix J, Banerdt W, Chenet H (2003) A new seismic model of the Moon: implication in terms of structure, formation, and evolution. *Earth Planet Sci Lett* 211:27–44
- Lognonné P, Le Feuvre M, Johnson C, Weber RC (2009) Moon meteoritic seismic hum: Steady state prediction. *J Geophys Res* 114:E12,003, DOI 10.1029/2008JE003294
- Lognonné P, Banerdt WB, Hurst K, Mimoun D, Garcia R, Lefeuvre M, Gagnepain-Beyneix J, Wieczorek M, Mocquet A, Panning M, Beucler E, Deraucourt S, Giardini D, Boschi L, Christensen U, Goetz W, Pike T, Johnson C, Weber R, Larmat K, Kobayashi N, Tromp J (2012) Insight and Single-Station Broadband Seismology: From Signal and Noise to Interior Structure Determination. In: *Lunar and Planetary Institute Science Conference Abstracts*, Lunar and Planetary Institute Science Conference Abstracts, vol 43, p 1983
- Lontsi AM, Sánchez-Sesma FJ, Molina-Villegas JC, Ohrnberger M, Krüger F (2015) Full microtremor H/V(z, f) inversion for shallow subsurface characterization. *Geophys J Int* 202:298–312, DOI 10.1093/gji/ggv132
- Malin MC, Edgett KS, Posiolova LV, McColley SM, Dobra EZN (2006) Present-day impact cratering rate and contemporary gully activity on Mars. *Science* 314:1573–1577
- Malischewsky P, Scherbaum F (2004) Love’s formula and H/V ratio (ellipticity) of Rayleigh waves. *Wave Motion* 40:57–67, DOI 10.1016/j.wavemoti.2003.12.015

- Matsumoto K, Yamada R, Kikuchi F, Kamata S, Ishihara Y, Iwata T, Hanada H, Sasaki S (2015) Internal structure of the Moon inferred from Apollo seismic data and selenodetic data from GRAIL and LLR. *Geophys Res Lett* 42:7351–7358, DOI 10.1002/2015GL065335
- McSween H (1994) What we have learned about Mars from SNC meteorites. *Meteoritics* 29:757–779
- Metropolis N, Rosenbluth A, Rosenbluth M, Teller A, Teller E (1953) Equation of state calculations by fast computing machines. *J Chem Phys* 21:1087–1091
- Mimoun D, Lognonné P, Banerdt WB, Hurst K, Deraucourt S, Gagnepain-Beyneix J, Pike T, Calcutt S, Bierwirth M, Roll R, Zweifel P, Mance D, Robert O, Nébut T, Tillier S, Laudet P, Kerjean L, Perez R, Giardini D, Christensen U, Garcia R (2012) The InSight SEIS Experiment. In: *Lunar and Planetary Institute Science Conference Abstracts*, Lunar and Planetary Institute Science Conference Abstracts, vol 43, p 1493
- Mimoun D, Murdoch N, Lognonné P, Pike WT, Hurst K, the SEIS Team (2016) The seismic noise model of the InSight mission to Mars. *Space Sci Rev* this volume
- Mocquet A, Vacher P, Grasset O, Sotin C (1996) Theoretical seismic models of Mars: the importance of the iron content of the mantle. *Planet Space Sci* 44:1251–1268
- Mohapatra RK, Murty SVS (2003) Precursors of Mars - constraints from nitrogen and oxygen isotopic compositions of martian meteorites. *Meteoritics and Planet Sci* 38:225–242
- Morgan JW, Anders E (1979) Chemical composition of Mars. *EOS Trans AGU* 60:306
- Mosegaard K, Tarantola A (1995) Monte-Carlo sampling of solutions to inverse problems. *J Geophys Res* 100:12,431–12,447
- Murdoch N, Mimoun D, Lognonné P, SEIS Science Team (2015) SEIS performance model environment document. Tech. Rep. ISGH-SEIS-JF-ISAE-0030, ISAE
- Murdoch N, Kenda B, Kawamura T, Spiga A, Lognonné P, Mimoun D, Banerdt WB (2016a) Estimations of the seismic pressure noise on Mars determined from Large Eddy Simulations and demonstration of pressure decorrelation techniques for the InSight mission. *Space Sci Rev* this volume
- Murdoch N, Mimoun D, Garcia RF, Rapin W, Kawamura T, Lognonné P (2016b) Evaluating the wind-induced mechanical noise on the InSight seismometers. *Space Sci Rev* this volume
- Nakamura Y (1983) Seismic velocity structure of the lunar mantle. *J Geophys Res* 88:677–686
- Nakamura Y (1989) A method for dynamic characteristics estimation of subsurface using microtremor on the ground surface. *Q Rep RTRI* 30:25–33
- Nakamura Y (2000) Clear identification of fundamental idea of Nakamura's technique and its applications. In: *Proceedings of the 12th World Conference on Earthquake Engineering*, Auckland
- Nakamura Y (2005) Farside deep moonquakes and deep interior of the Moon. *J Geophys Res* 110:E01,001, DOI 10.1029/2004JE002332

- Nakamura Y (2008) On the H/V spectrum. In: Proceedings of the 14th World Conference on Earthquake Engineering, Beijing
- Nakamura Y, Anderson D (1979) Martian wind activity detected by a seismometer at Viking Lander 2 site. *Geophys Res Lett* 6:499–502, DOI 10.1029/GL006i006p00499
- Nakamura Y, Dorman J, Duennebieer F, Lammlein D, Latham G (1975) Shallow lunar structure determined from the passive seismic experiment. *The Moon* 13:57–66
- Nakamura Y, Latham G, Dorman H, Ibrahim AB, Koyama J, Horvarth P (1979) Shallow moonquakes - depth, distribution and implications as to the present state of the lunar interior. In: Proc. Lunar Planet. Sci. Conf. 10th, pp 2299–2309
- Neumann G, Zuber M, Wieczorek M, McGovern P, Lemoine F, Smith D (2004) Crustal structure of Mars from gravity and topography. *J Geophys Res* 109(E8):E08,002, DOI 10.1029/2004JE002262
- Nimmo F, Faul UH (2013) Dissipation at tidal and seismic frequencies in a melt-free, anhydrous Mars. *J Geophys Res* 118(12):2558–2569, DOI 10.1002/2013JE004499, URL <http://dx.doi.org/10.1002/2013JE004499>
- Nishikawa et al (2016) Title to be completed. *Space Sci Rev* this volume
- Nissen-Meyer T, van Driel M, Stähler SC, Hosseini K, Hempel S, Auer L, Colombi A, Fournier A (2014) AxiSEM: broadband 3-D seismic wavefields in axisymmetric media. *Solid Earth* 5(1):425–445
- Okal EA, Anderson DL (1978) Theoretical models for Mars and their seismic properties. *Icarus* 33:514–528, DOI 10.1016/0019-1035(78)90187-2
- Oldham RD (1906) The constitution of the interior of the Earth, as revealed by earthquakes. *Quar J Geol Soc* 62(1–4):456–475
- Panning MP, Beucler E, Drilleau M, Mocquet A, Lognonné P, Banerdt WB (2015) Verifying single-station seismic approaches using Earth-based data: Preparation for data return from the InSight mission to Mars. *Icarus* 248:230–242, DOI 10.1016/j.icarus.2014.10.035
- Panou A, Theodulidis N, Hatzidimitriou P, Stylianidis K, Papazachos C (2005) Ambient noise horizontal-to-vertical spectral ratio in site effects estimation and correlation with seismic damage distribution in urban environment: the case of the city of Thessaloniki (Northern Greece). *Soil Dyn Earthq Eng* 25:261–274, DOI 10.1016/j.soildyn.2005.02.004
- Park J, Levin V (2000) Receiver functions from multiple-taper spectral correlation estimates. *Bull Seism Soc Am* 90(6):1507–1520
- Park J, Lindberg CR, Thomson DJ (1987) Multiple-taper spectral analysis of terrestrial free oscillations: part I. *Geophys J Int* 91(3):755–794, DOI 10.1111/j.1365-246X.1987.tb01668.x
- Phillips R (1991) Expected rate of marsquakes. In: Scientific Rationale and Requirements for a Global Seismic Network on Mars, LPI Tech. Rept., 91-02, Lunar and Planetary Inst., Houston, pp 35–38
- Pivarunas A, Warner NH, Golombek MP (2015) Onset diameter of rocky ejecta craters in western Elysium Planitia, Mars: Constraints for regolith thickness at the InSight landing site. In: 46th Lunar and Planetary Science Confer-

- ence, Lunar and Planetary Inst., Houston, TX, p Abstract # 1129, URL <http://www.hou.usra.edu/meetings/lpsc2015/pdf/1129.pdf>
- Plesa AC, Grott M, Tosi N, Breuer D, Spohn T, Wieczorek M (2016) How large are present-day heat flux variations across the surface of Mars? *J Geophys Res* DOI 10.1002/2016JE005126, accepted
- Plescia JB (1990) Recent flood lavas in the Elysium region of Mars. *Icarus* 88:465–490
- Poggi V, Fäh D, Burjanek J, Giardini D (2012) The use of Rayleigh-wave ellipticity for site-specific hazard assessment and microzonation: application to the city of Lucerne, Switzerland. *Geophys J Int* 188:1154–1172, DOI 10.1111/j.1365-246X.2011.05305.x
- Press F (1968) Earth models obtained by Monte Carlo inversion. *J Geophys Res* 73:5223–5234, DOI 10.1029/JB073i016p05223
- Quiros DA, Brown LD, Kim D (2016) Seismic interferometry of railroad induced ground motions: body and surface wave imaging. *Geophys J Int* 205:301–313, DOI 10.1093/gji/ggw033
- Richardson JE, Melosh HJ, Greenberg RJ, O'Brien DP (2005) The global effects of impact-induced seismic activity on fractured asteroid surface morphology. *Icarus* 179:325–349
- Rivoldini A, Van Hoolst T (2013) The interior structure of Mercury constrained by the low-degree gravity field and the rotation of Mercury. *Earth Planet Sci Lett* 377–378:67–72, DOI 10.1016/j.epsl.2013.07.021
- Rivoldini A, Van Hoolst T, Verhoeven O, Mocquet A, Dehant V (2011) Geodesy constraints on the interior structure and composition of Mars. *Icarus* 213:451–472
- Roberts GP, Matthews B, Bristow C, Guerrieri L, Vetterlein J (2012) Possible evidence of paleomarsquakes from fallen boulder populations, Cerberus Fossae, Mars. *J Geophys Res* 117(E2):E003,816
- Rost S, Thomas C (2009) Improving seismic resolution through array processing techniques. *Surveys Geophys* 30:271–299
- Sambridge M (1999) Geophysical inversion with a neighbourhood algorithm - I. searching a parameter space. *Geophys J Int* 138:479–494, DOI 10.1046/j.1365-246X.1999.00876.x
- Sánchez-Sesma FJ, Crouse CB (2015) Effects of site geology on seismic ground motion: Early history. *Earthq Eng Struct Dyn* 44:1099–1113, DOI 10.1002/eqe.2503
- Sánchez-Sesma FJ, Rodríguez M, Iturrarán-Viveros U, Luzón F, Campillo M, Margerin L, García-Jerez A, Suarez M, Santoyo MA, Rodríguez-Castellanos A (2011) A theory for microtremor H/V spectral ratio: application for a layered medium. *Geophys J Int* 186:221–225, DOI 10.1111/j.1365-246X.2011.05064.x
- Sanloup C, Jambon A, Gillet P (1999) A simple chondritic model of Mars. *Phys Earth Planet Int* 112:43–54
- Scherbaum F, Hinzen KG, Ohrnberger M (2003) Determination of shallow shear wave velocity profiles in the Cologne, Germany area using ambient vibrations. *Geophys J Int* 152:597–612, DOI 10.1046/j.1365-

- 246X.2003.01856.x
- Schmerr NC, Kelly BM, Thorne MS (2013) Broadband array observations of the 300 km seismic discontinuity. *Geophys Res Lett* 40(5):841–846
- Schweitzer J, Fyen J, Mykkeltveit S, Kværna T (2002) Seismic arrays. In: Bormann P (ed) *IASPEI New Manual of Seismological Observatory Practice*, GFZ German Research Center for Geosciences, Potsdam
- Shapiro N, Ritzwoller M (2002) Monte-Carlo inversion for a global shear-velocity model of the crust and upper mantle. *Geophys J Int* 151:88–105
- Shearer P (2009) *Introduction to Seismology*. Cambridge Univ. Press, Cambridge, U.K.
- Sohl F, Spohn T (1997) The interior structure of Mars: Implications from SNC meteorites. *J Geophys Res* 102(E1):1613–1635
- Spohn T, Grott M, Smrekar S, Krause C, Hudson TL, the HP³ instrument team (2014) Measuring the martian heat flow using the heat flow and physical properties package (HP³). In: #1916 A (ed) 45th Lunar and Planetary Science Conference, Lunar and Planetary Inst., Houston, TX, URL <http://www.hou.usra.edu/meetings/lpsc2014/pdf/1916.pdf>
- Steinberger B, Zhao D, Werner SC (2015) Interior structure of the Moon: Constraints from seismic tomography, gravity and topography. *Physics of the Earth and Planetary Interiors* 245:26–39, DOI 10.1016/j.pepi.2015.05.005
- Stixrude L, Lithgow-Bertelloni C (2011) Thermodynamics of mantle minerals - II. phase equilibria. *Geophys J Int* 184(3):1180–1213, DOI 10.1111/j.1365-246X.2010.04890.x
- Takashi R, Hirano K (1941) Seismic vibrations of soft ground (in japanese). *Bull Earthq Res Inst* 19:534–543
- Tanimoto T, Rivera L (2008) The zh ratio method for long-period seismic data: sensitivity kernels and observational techniques. *Geophys J Int* 172(1):214–219
- Tanimoto T, Eitzel M, Yano T (2008) The noise cross-correlation approach for Apollo 17 LPSE data: Diurnal change in seismic parameters in the shallow lunar crust. *J Geophys Res* 113:E08,011, DOI 10.1029/2007JE003016
- Taylor GJ (2013) The bulk composition of Mars. *Chemie der Erde - Geochem* 73(4):401–420, DOI 10.1016/j.chemer.2013.09.006
- Taylor J, Teanby NA, Wookey J (2013) Estimates of seismic activity in the Cerberus Fossae region of Mars. *J Geophys Res* E118:2570–2581
- Teanby NA (2015) Predicted detection rates of regional-scale meteorite impacts on Mars with the InSight short-period seismometer. *Icarus* 256:49–62
- Teanby NA, Wookey J (2011) Seismic detection of meteorite impacts on Mars. *Phys Earth Planet Int* 186:70–80
- Teanby NA, Stevanović J, Wookey J, Murdoch N, Hurley J, Myhill R, Bowles NE, Calcutt SB, Pike WT (2016) Seismic coupling of short-period wind noise through Mars' regolith for NASA's InSight lander. *Space Sci Rev* this volume
- Thomson W (1863) On the rigidity of the Earth. *Phil Trans R Soc Lond* 153:573–582, DOI 10.1098/rstl.1863.0027

- Van Hoolst T, Dehant V, Roosbeek F, Lognonné P (2003) Tidally induced surface displacements, external potential variations, and gravity variations on Mars. *Icarus* 161(2):281–296, DOI 10.1016/S0019-1035(02)00045-3
- Vaucher JD, Baratoux D, Mangold N, Pinet P, Kurita K, Grégoire M (2009) The volcanic history of central Elysium Planitia: Implications for martian magmatism. *Icarus* 204:418–442
- Verhoeven O, Rivoldini A, Vacher P, Mocquet A, Choblet G, Menvielle M, Dehant V, Van Hoolst T, Sleewaegen J, Barriot JP, Lognonné P (2005) Interior structure of terrestrial planets: Modeling Mars' mantle and its electromagnetic, geodetic, and seismic properties. *J Geophys Res* 110:E04,009, DOI 10.1029/2004JE002271
- Vetterlein J, Roberts GP (2010) Structural evolution of the Northern Cerberus Fossae graben system, Elysium Planitia, Mars. *J Struct Geol* 32:394–406, DOI 10.1016/j.jsg.2009.11.004
- Vinciguerra S, Trovato C, Meredith PG, Benson PM (2005) Relating seismic velocities, thermal cracking and permeability in Mt. Etna and Iceland basalts. *Int J Rock Mech Min Sci* 42:900–910, DOI 10.1016/j.ijrmms.2005.05.022
- Vinnik L, Chenet H, Gagnepain-Beyneix J, Lognonné P (2001) First seismic receiver functions on the Moon. *Geophys Res Lett* 28:3031–3034
- Von Rebeur-Paschwitz E (1889) The earthquake of Tokio 18 April 1889. *Nature* 40:294–295, DOI 10.1038/040294e0
- Warner N, Golombek MP, Sweeney J, Fergason R, Kirk R, Schwartz C (2016) Near surface stratigraphy and regolith production in southwestern Elysium Planitia, Mars: Implications of Hesperian-Amazonian terrains and the In-Sight lander mission. *Space Sci Rev* this volume
- Wathelet M (2008) An improved neighborhood algorithm: Parameter conditions and dynamic scaling. *Geophys Res Lett* 35:L09,301, DOI 10.1046/j.1365-246X.19993.00876.x
- Wathelet M, Jongmans D, Ohrnberger M (2004) Surface-wave inversion using a direct search algorithm and its application to ambient vibration measurements. *Near Surf Geophys* 2:211–221
- Weber R, Lin PY, Garner E, Williams Q, Lognonné P (2011) Seismic detection of the lunar core. *Science* 331(6015):309–312
- Wells SG, Dohrenwend JC, McFadden LD, Turrin BD, Mahrer KD (1985) Late Cenozoic landscape evolution on lava flow surfaces of the Cima volcanic field, Mojave Desert, California. *Geol Soc Am Bull* 96:1518–1529
- Wieczorek M, Zuber M (2004) Thickness of the Martian crust: Improved constraints from geoid-to-topography ratios. *J Geophys Res* 109:E01,009, DOI 10.1029/2003JE002153
- Williams DR (2016) URL <http://nssdc.gsfc.nasa.gov/planetary/factsheet/marsfact.html>
- Williams JP, Pathare AV, Aharonson O (2014) The production of small primary craters on Mars and the Moon. *Icarus* 235:23–36
- Woodhouse J (1988) The calculation of eigenfrequencies and eigenfunctions of the free oscillations of the earth and the sun. In: Doornbos D (ed) *Seismological Algorithms*, Academic Press, London, pp 321–370

-
- Zhao D, Arai T, Liu L, Ohtani E (2012) Seismic tomography and geochemical evidence for lunar mantle heterogeneity: Comparing with Earth. *Global and Planetary Change* 90:29–36, DOI 10.1016/j.gloplacha.2012.01.004
- Zharkov VN, Gudkova TV (1997) On the dissipative factor of the martian interiors. *Planet Space Sci* 45:401–407
- Zharkov VN, Gudkova TV, Molodensky SM (2009) On models of Mars' interior and amplitudes of forced nutations: 1. the effects of deviation of Mars from its equilibrium state on the flattening of the core–mantle boundary. *Phys Earth Planet Int* 172:324–334, DOI 10.1016/j.pepi.2008.10.009
- Zheng Y, Nimmo F, Lay T (2015) Seismological implications of a lithospheric low seismic velocity zone in Mars. *Phys Earth Planet Int* 240:132–141, DOI 10.1016/j.pepi.2014.10.004

Table 1 Major element composition (weight percent) models.

	MAK ¹	DW ²	LF ³	EH45 ⁴	MM ⁵
CaO	5.2	2.4	2.4	2.0	1.9
FeO	15.80	17.9	17.2	17.7	16.9
MgO	29.80	30.2	29.7	27.3	29.1
Al ₂ O ₃	6.40	3.0	2.9	2.5	2.5
SiO ₂	41.6	44.4	45.4	47.5	47.1
Na ₂ O	0.1	0.5	0.98	1.2	1.2

¹ (Morgan and Anders, 1979)² (Dreibus and Wänke, 1985)³ (Lodders and Fegley, 1997)⁴ (Sanloup et al, 1999)⁵ (Mohapatra and Murty, 2003)**Table 2** Subsurface model used to generate synthetic hammer derived seismograms.

Thickness (m)	V_P (m/s)	V_S (m/s)	ρ (kg/m ³)	Q_P
50 m	300	173	1500	50
Half-space	2000	1154	2700	100

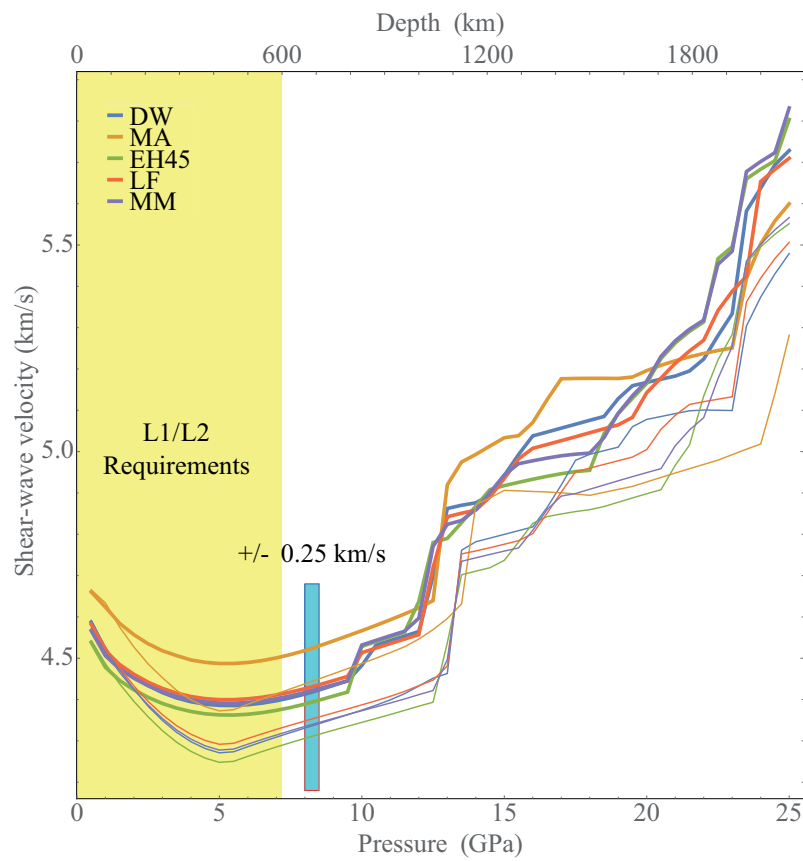


Fig. 1 A suite of predicted shear wave velocity models for the mantle under Mars conditions for a series of bulk composition models. For each composition, the thick line represents calculated properties for a cold thermal profile, while the thin one represents a hot profile (Plesa et al, 2016). Temperature profiles are shown in figure 2. Composition model abbreviations are defined in table 1. Light blue colored bar represents the L1 and L2 mission requirements for InSight’s ability to resolve elastic structure. The L1-L2 requirements are defined only for the depth region shaded in yellow.

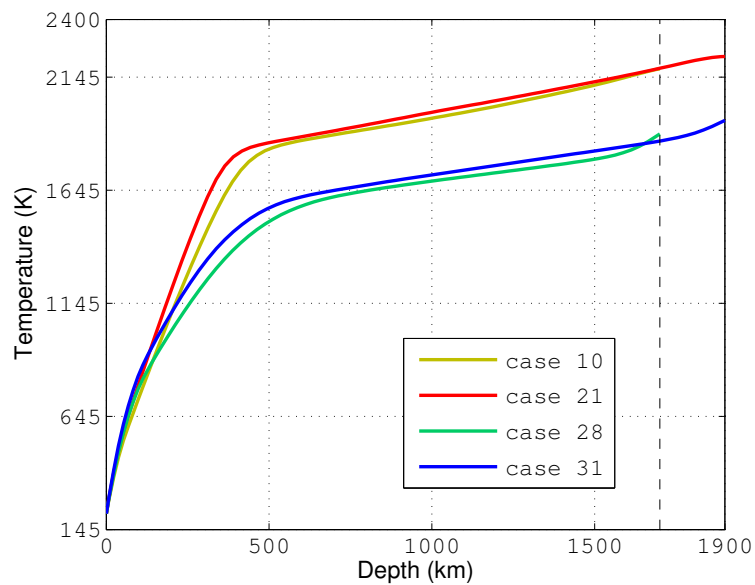


Fig. 2 Present-day cold and hot end member temperature profiles obtained from thermal evolution models. Case 10 and case 21 from (Plesa et al, 2016) use a reference viscosity of $10^{21} Pa s$ and a large increase of viscosity with depth (i.e., an activation volume of $10 cm^3/mol$) while case 28 and case 31 use a reference viscosity of $10^{20} Pa s$ and a moderate increase of viscosity with depth (i.e., an activation volume of $6 cm^3/mol$). Moreover, case 10 and case 21 have an average crustal thickness of about $45 km$, while the cases 28 and 31 use a thicker crust ($\sim 87 km$) and hence have a mantle more depleted in radiogenic elements. The cases with a mantle thickness of $1700 km$ (case 10 and case 28) employ two exothermic phase transitions, while for the cases with a mantle thickness of $1900 km$ an additional endothermic phase transition has been considered. The models of figure 1 use the $1900 km$ profiles. For a detailed description of the thermal evolution models we refer the reader to Plesa et al (2016).

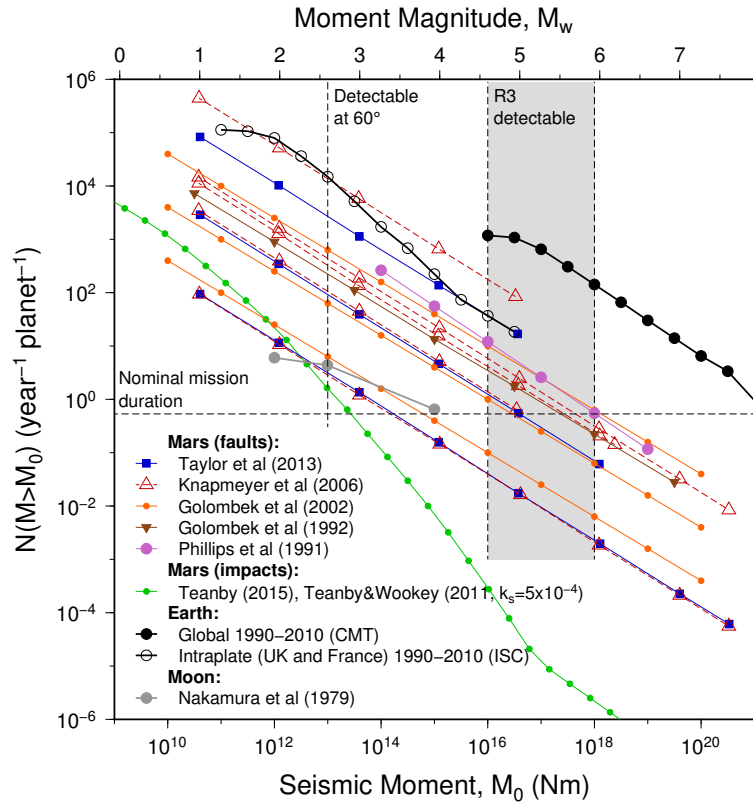


Fig. 3 Predictions of martian seismicity for faults and impacts. Mars faulting estimates are based on Phillips (1991); Golombek et al (1992); Golombek (2002); Knapmeyer et al (2006) (global) and Taylor et al (2013) (Cerberus Fossae only). Impact seismicity is based on Teanby (2015)'s nominal regional estimates and Teanby and Wookey (2011)'s global estimates with a revised seismic efficiency of $k = 5 \times 10^{-4}$. For comparison the seismicity is also shown for the Moon (Nakamura et al, 1979) and Earth (whole globe from Harvard CMT catalogue and Intraplate settings from ISC catalogue). The dashed vertical line shows the threshold magnitude for a detection at 60° offset based on the InSight seismometer performance and waveform modeling (Teanby and Wookey, 2011). The grey shaded area shows the threshold magnitude for detection of the R3 surface wave, which will allow source-receiver distance calculations (Panning et al, 2015). Horizontal dashed line indicates mission duration of 1 Mars year (2 Earth years).

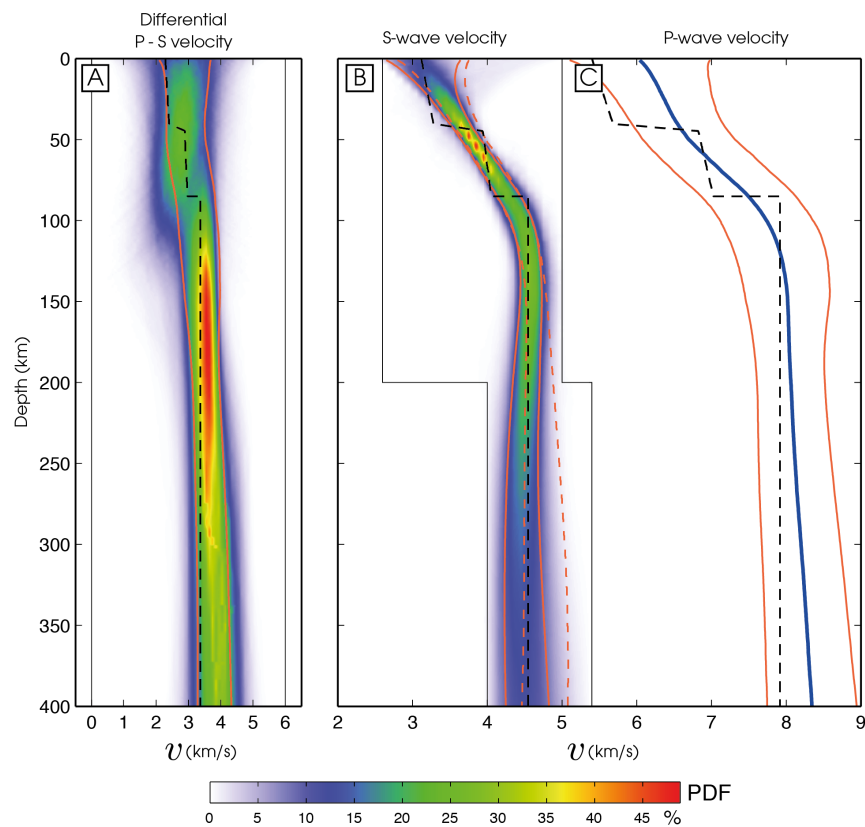


Fig. 4 Inversion results. The black dashed lines show the model to retrieve. (a) and (b) show *a posteriori* probability density functions (PDF) of differential $V_P - V_S$ velocity and of S wave velocity. Red and blue colors show high and low probabilities, respectively. Continuous black lines represent the minimum and maximum parameter values allowed. Orange curves delimit the interval between $\pm 1\sigma$ of the median profile of the distribution. $S - P$ travel times are used to constraint the differential $V_P - V_S$ velocity (a), while surface wave dispersion is used to determine V_S (b). In (b), the orange dashed lines represent the interval between $\pm 1\sigma$ of the V_S distribution obtained using the noisy synthetic data. The mean V_P profile (blue line in c) and $\pm 1\sigma$ standard deviation (in orange) is estimated from the PDFs in (a) and (b).

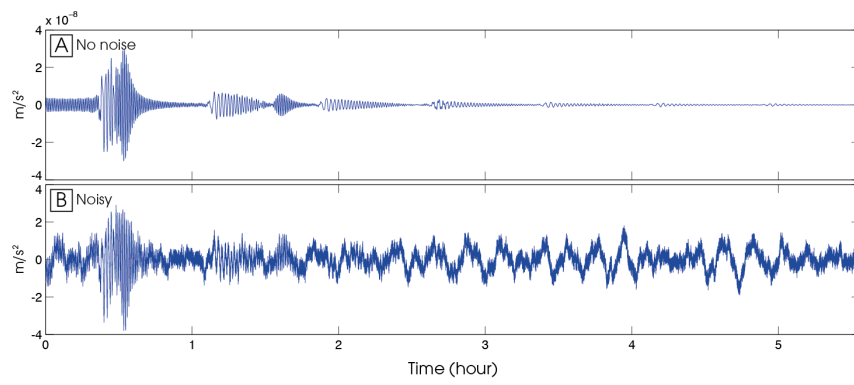


Fig. 5 Example synthetic seismograms computed using the normal mode code MINEOS (e.g. Woodhouse, 1988) with no noise (a) and including the noise model of Mimoun et al (2016) (b) for a M_W 6.0 event at 45° distance.

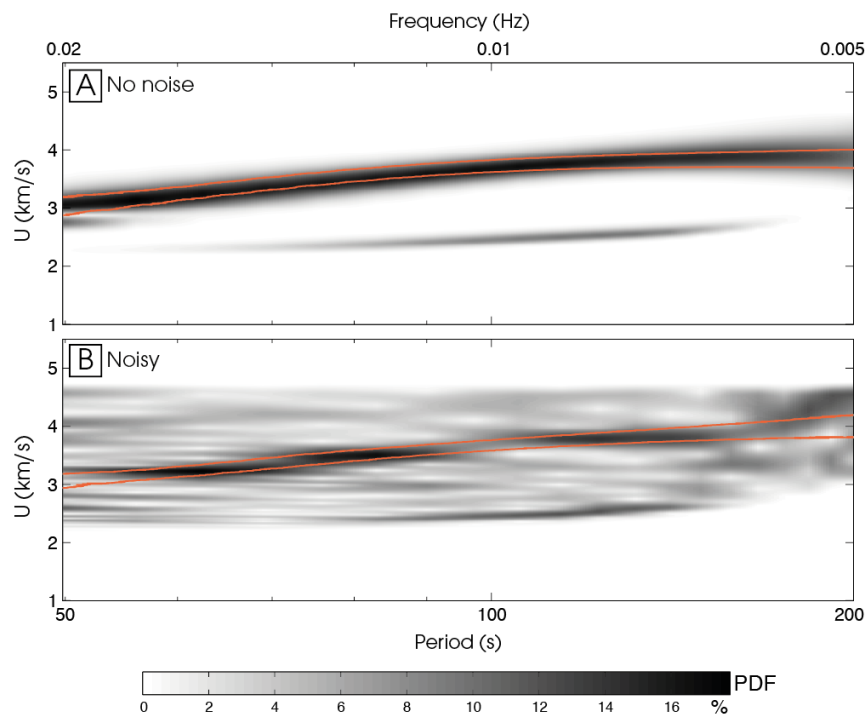


Fig. 6 Synthetic input dispersion diagrams computed with the seismic model shown in fig. 4, with no noise (a) and noise (b). The gray scale represents the probability density function assigned to each group velocity value at a given frequency. Black and white show high and low probabilities, respectively. Orange curves circumscribe the predicted group velocity values of all the models accepted by the MCMC inversion.

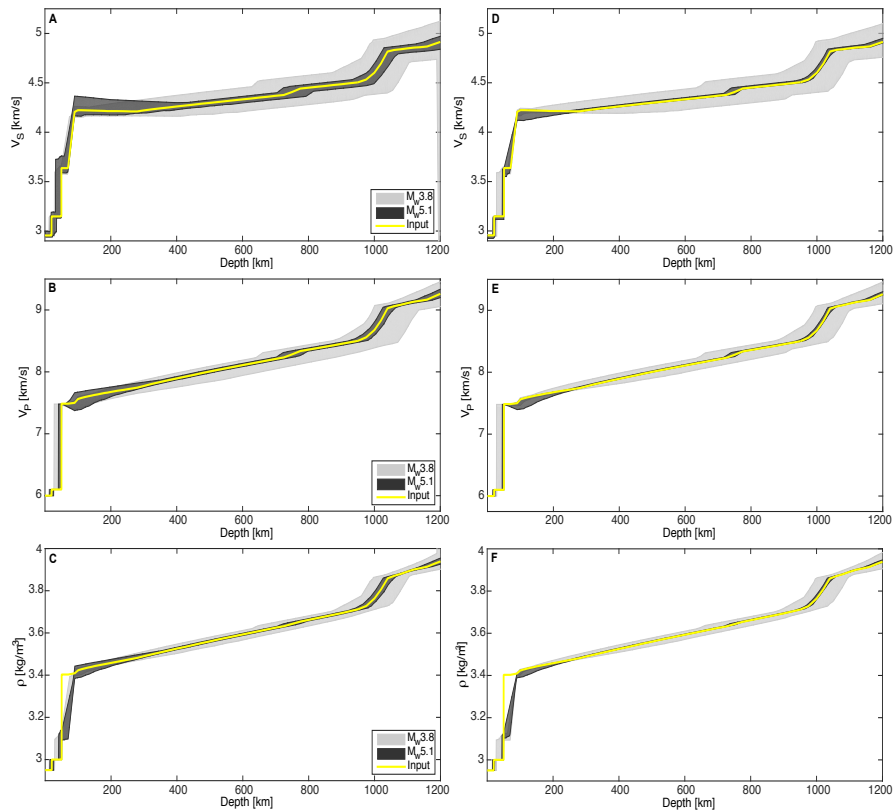


Fig. 7 “Preliminary” (a–c) and “Final” (d–f) inverted martian models. Shown are profiles of S-wave speed (a, d), P-wave speed (b, e), and density (c, f). Envelopes encompass all sampled models. Input designates the input model employed for computing martian seismograms. “Preliminary” inverted models are based on dispersion and P- and S-wave travel time data. “Final” inverted models are based on dispersion and the expanded travel time data set. The $M_W5.1$ event is located at an epicentral distance of 86.6° as a result of which rays sample deeper than in the case of the regional $M_W3.8$ event (27.6°). Figure from Khan et al (2016).

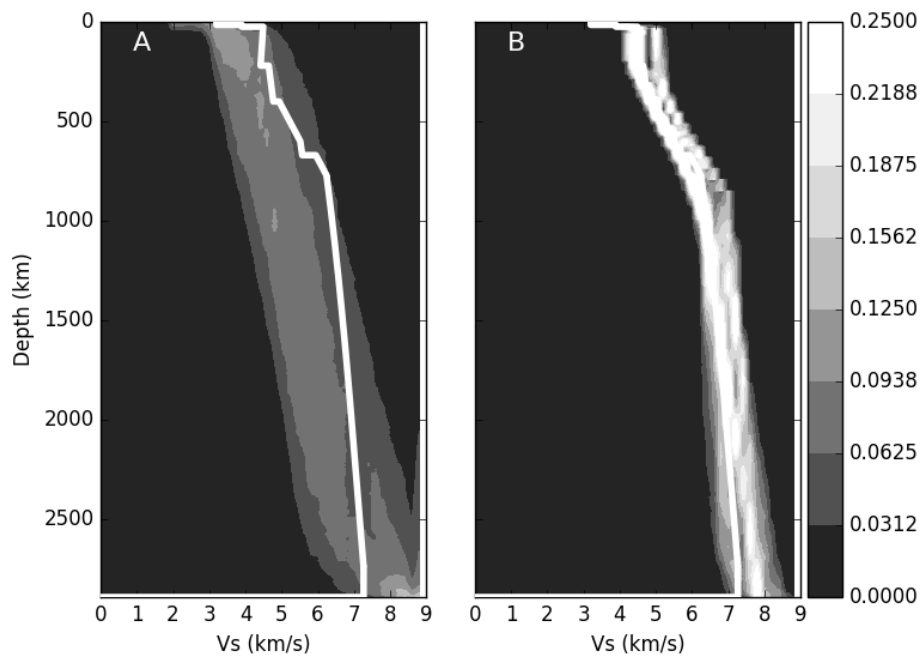


Fig. 8 Prior (a) and posterior (b) probability density functions for a Bayesian McMC inversion of synthetic Earth data from 5 events between 500 and 8000 *km* distance. The data were calculated from the model PREM (white line, Dziewonski and Anderson, 1981).

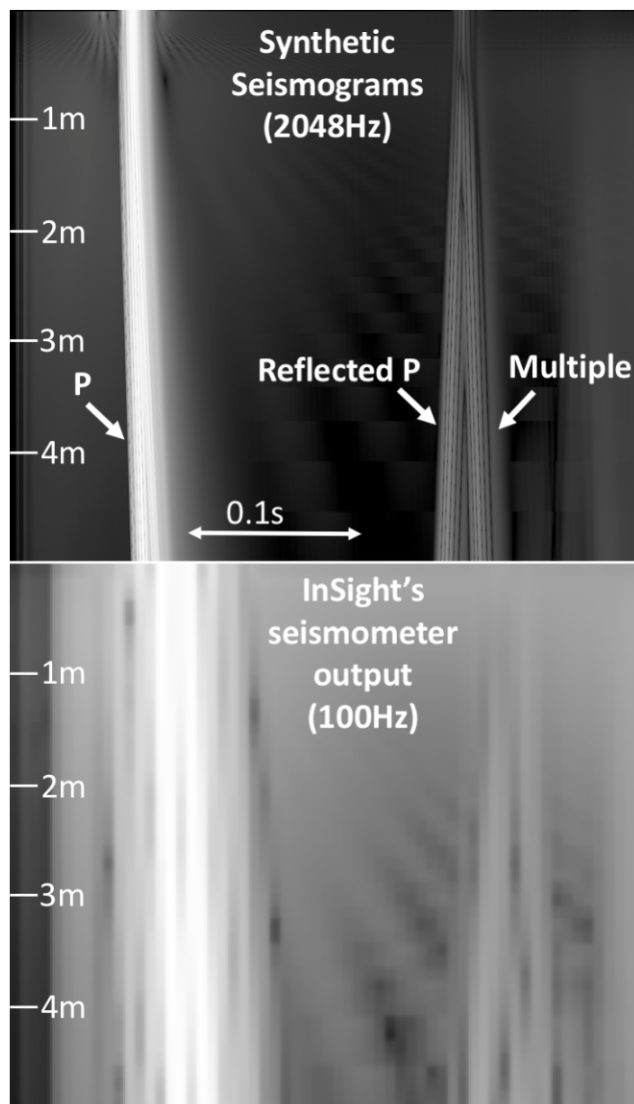


Fig. 9 Composite image made of 5000 seismograms at high resolution (top, 2048 Hz) and as they would be observed by InSight (bottom, 100 Hz). For visual enhancement, each seismic trace is self-normalized against its maximum energy and the color scales based on the logarithm of energy. The lighter appearance of the decimated data (bottom) is a manifestation of the smearing of the energy through decimation. At each depth along the vertical axis, the amplitude variation in time along the horizontal axis represents a single seismogram calculated for the hammering at that depth.

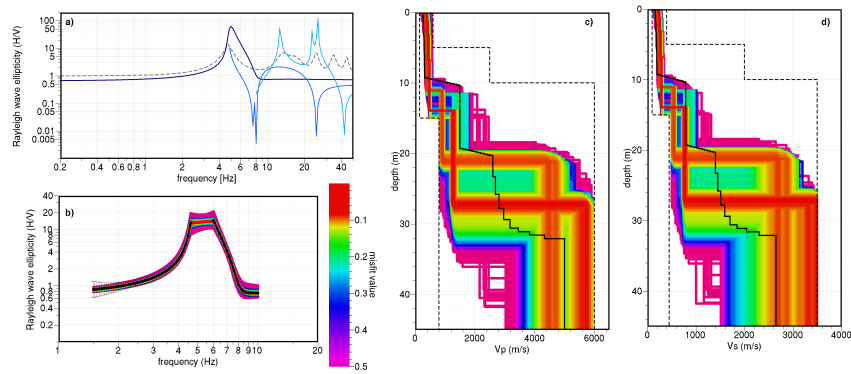


Fig. 10 a) Forward calculated ellipticity curves (blue curves) and SH response function (dashed black curve) for a reasonable velocity model based on orbital measurements and crater ejecta analysis. From dark to light blue, the ellipticity functions for the first three Rayleigh wave modes are shown. b) Fit to the inverted data (left and right flank of the ellipticity peak, shown as black curves with error bars) for an inversion with a simple three-layer parameterization. c) P-wave velocity models resulting from the inversion. Black curve is the input model for the forward calculations, and dashed lines mark the boundaries of the parameter space in the inversion. d) Same as c) for S-wave velocities.

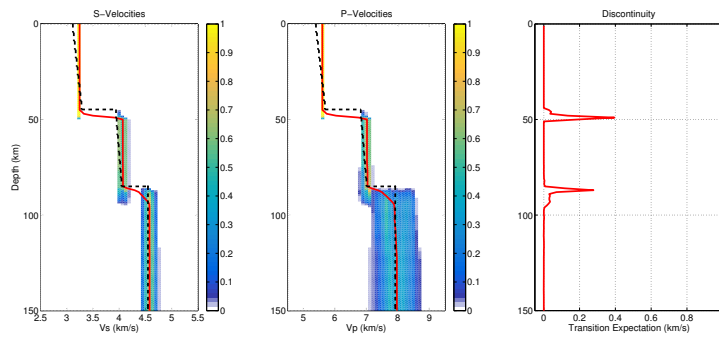


Fig. 11 Probability density functions (PDFs) for V_S (left) and V_P (middle) obtained from a Bayesian inversion of synthetic receiver functions combined with surface wave ellipticity measurements. The right panel shows discontinuity transition expectation, which is the product of the probability of a jump at a given depth with the average shear velocity change of the jump. The input model is shown by the black dashed line, and the mean model from each PDF is shown with a red line.

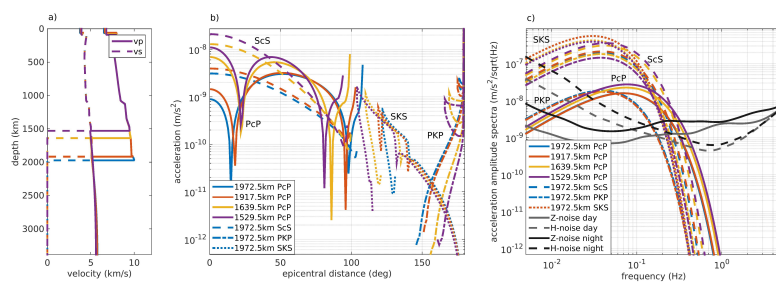


Fig. 12 Ray theoretical spectral ground acceleration amplitude predictions for seismic phases reflected at the core-mantle boundary (PcP, ScS) or transmitted through the core of Mars (PKP, SKS) for a surface source with a seismic moment of 10^{16} Nm ($M_W 4.6$). a) Seismic velocity profiles for various core sizes based on the bulk composition model of Dreibus and Wänke (1985) (fig. 1) for the amplitude, travel-time and ray parameter predictions in figures 12 and 13. (b) Amplitudes as predicted by ray theory with respect to epicentral distance at frequencies of 0.25 Hz . The minima in PcP amplitude at 25° to 30° , and 85° to 105° epicentral distance correspond to a phase shift in the complex reflection coefficient for reflections at the core mantle boundary. (c) Ground acceleration amplitude spectra of PcP, PKP, horizontally polarized ScS and vertically polarized SKS signals for the models in (a) at 60° epicentral distance for core-reflected phases PcP and ScS, and at 170° epicentral distances for core-transmitted phases PKP and SKS. Black and grey lines mark the mean InSight lander noise (Mimoun et al, 2016, this issue).

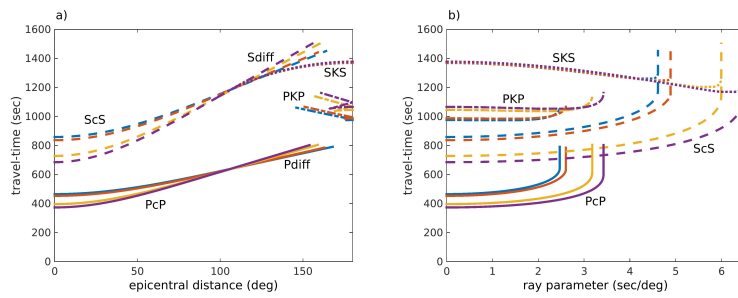


Fig. 13 Travel-time as a function of epicentral distance and ray parameter for PcP and Pdiff, PKP, ScS and Sdiff signals as well as SKS for a surface source. Travel-times are computed for bulk compositions as in figure 12 with various core sizes as shown in figure 12a. (a) Absolute travel-times as a function of epicentral distance. (b) Travel-times as a function of ray parameter, which can be determined through polarization analysis of a phase arrival at a three-component station. Maximum ray parameters for PcP/ PKP/ Pdiff and ScS/ SKS/ Sdiff are a function of the core size.

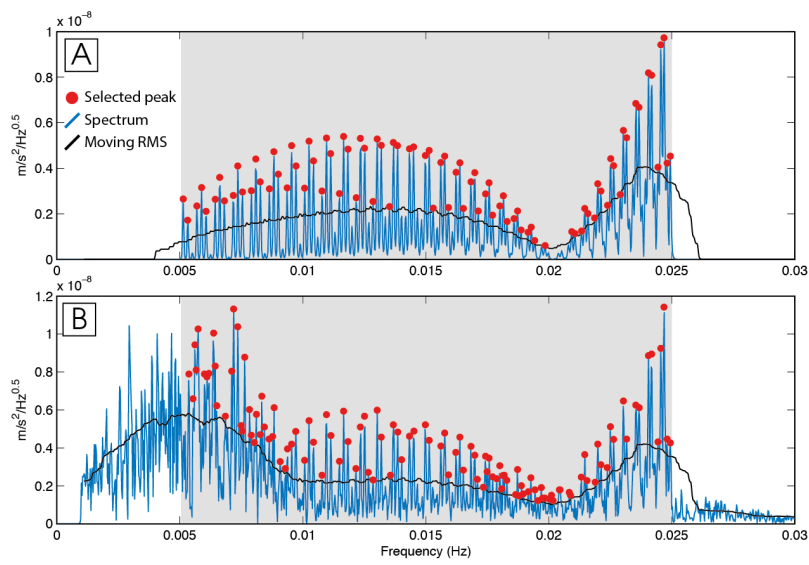


Fig. 14 Noise-free (a) and noisy (b) spectra used to compute the eigenfrequencies used in the inversions. Only the peaks with an amplitude larger than a moving RMS (black line) are considered. These are shown in red.

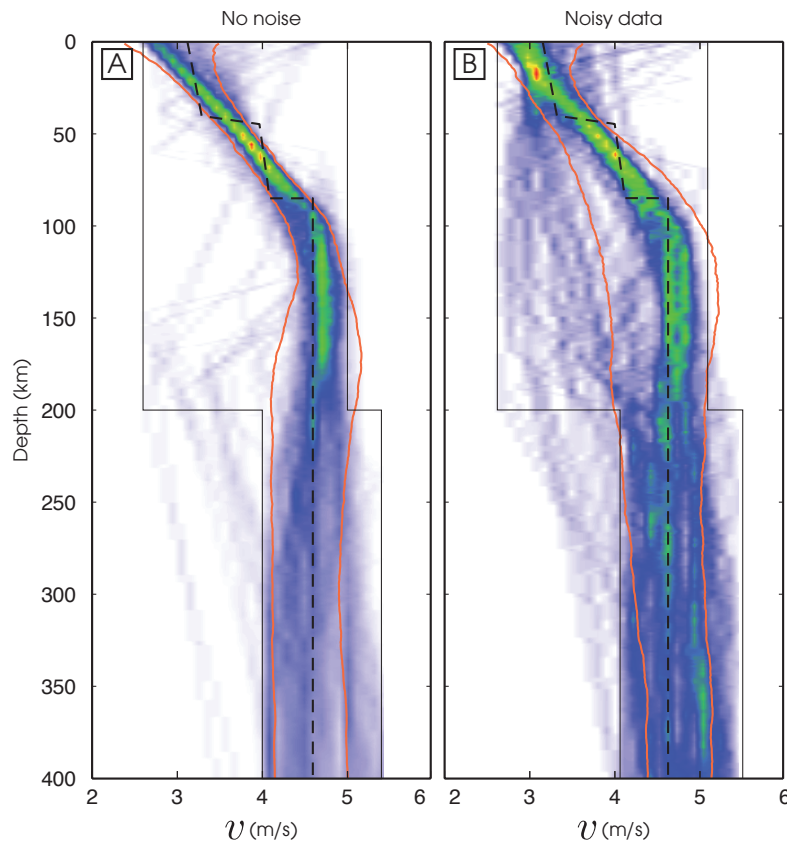


Fig. 15 Results of the normal mode inversion. The black dashed lines show the model to retrieve. (a) and (b) show *a posteriori* probability density functions (PDF) of S wave velocity. Red and blue colors show high and low probabilities, respectively. Continuous black lines represent the minimum and maximum parameter values allowed. Orange curves delimit the interval between $\pm 1\sigma$ of the median profile of the distribution. (a) and (b) are the results from the inversion of eigenfrequencies with no noise and including noise, respectively.

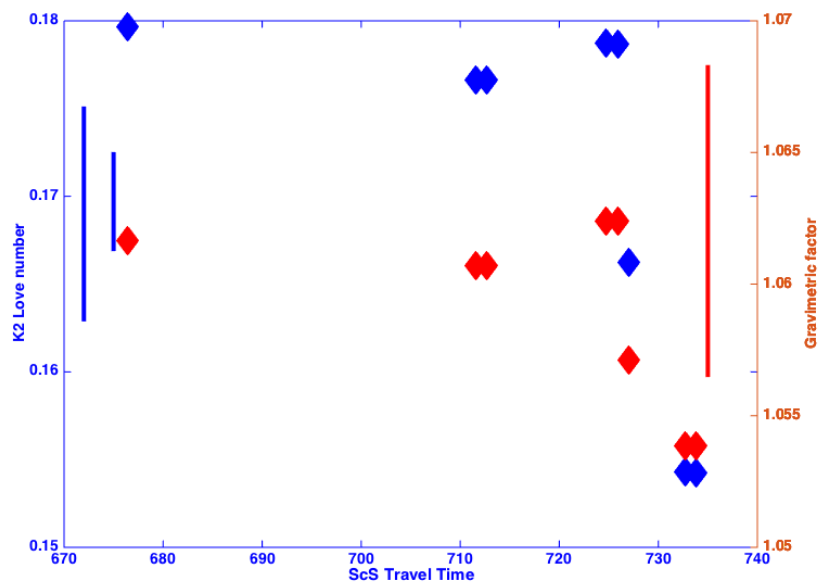


Fig. 16 Models are arranged by increasing ScS travel times and are from left to right: EH45Cold without crust, DWThotCrust1, DWThotCrust1r, EH45ThotCrust2, EH45ThotCrust2r, DWThot, EH45TcoldCrust1 and EH45TcoldCrust1r. Models with r have a thin layer of 1 km bedrock below an 80 m regolith. Crust1 and Crust2 have different crustal structure. DW mantle bulk composition is from Taylor (2013), while EH45 mantle bulk composition is from Sanloup et al (1999). Hot and cold temperature profiles are from Plesa et al (2016) (fig. 2). The resolution of ScS picking will mainly depend on the attenuation of these waves and will likely be much better than 5 s. If detected, ScS will therefore be a much stronger constraint, but the gravimetric factors and Love number will nevertheless be able to separate models with similar ScS, as shown for the EH45ThotCrust2, DWThot and EH45TcoldCrust1 on the right side of the figure. The left blue bar is the range for the k_2 measurement from Konopliv et al (2016), while the right red bar is the error bar for an $\pm 0.5\%$ error in the tide measurement.